Microstructure-statistics-property relations of anisotropic polydisperse particulate composites using tomography

A. Gillman, K. Matouš,[*] and S. Atkinson

Department of Aerospace and Mechanical Engineering, University of Notre Dame, Notre Dame, Indiana 46556, USA

In this paper, a systematic method is presented for developing microstructure-statistics-property relations of anisotropic polydisperse particulate composites using microcomputer tomography (micro-CT). Micro-CT is used to obtain a detailed three-dimensional representation of polydisperse microstructures, and an image processing pipeline is developed for identifying particles. In this work, particles are modeled as idealized shapes in order to guide the image processing steps and to provide a description of the discrete micro-CT data set in continuous Euclidean space. n-point probability functions used to describe the morphology of mixtures are calculated directly from real microstructures. The statistical descriptors are employed in the Hashin-Shtrikman variational principle to compute overall anisotropic bounds and self-consistent estimates of the thermal-conductivity tensor. We make no assumptions of statistical isotropy nor ellipsoidal symmetry, and the statistical description is obtained directly from micro-CT data. Various mixtures consisting of polydisperse ellipsoidal and spherical particles are prepared and studied to show how the morphology impacts the overall anisotropic thermal-conductivity tensor.

I. INTRODUCTION

Understanding the packing of various particulate systems is critical to a variety of scientific fields including biology, material science, geophysics, chemistry, and engineering with applications including but not limited to amorphous solids [1], heterogeneous materials [2,3], geological formations [4], protein configurations [5], pharmaceutical powders [6], and agricultural products [7]. Much of the work related to characterizing and modeling these systems has been dedicated to idealized isotropic packs composed most often of spheres. However, for many of these systems, rarely are the particles spherical and the morphologies isotropic, and the physical implications of these assumptions are not fully understood. In the study of the glass transition state for the formation of amorphous (glassy) solids, the ideal sphere model, where molecules are modeled as monodisperse spheres, is well understood. However, as pointed out in the review by Liu and Nagel [8], an ideal sphere model likely resembles real glass forming systems the least as molecules are not spherical. The particle shape also plays a key role in the flow, compaction, and mechanical loading of granular systems, e.g., sand, soil, etc. In the work of Cleary and Sawley [9], discrete element simulations show that grain shape has a substantial impact on the overall flow rates and local flow behavior of particles in hoppers. However, assumptions are made about the distribution of particle sizes and shapes without justification based on real morphologies. Experimental analysis of the compaction process through tapping shows that nonspherical shapes have a tendency to align, illustrating that manufacturing steps of particulate materials, for example, can result in anisotropic configurations. Fu *et al.* [10] studied the changing morphology of a system of rods in compaction experiments and revealed larger degrees of rod alignment with increased tapping times. An additional experimental study of granular systems by Ribièri *et al.* [11] revealed that the tapping acceleration used for compacting

systems of basmati rice (polydisperse nonspherical particles) plays a critical role in the types of convective flows that develop, thereby affecting the final structures that form. Such granular flows and compaction phenomena are critical among other applications to modeling manufacturing procedures. For example, an uneven burning profile is observed in solid propellants due to particle alignment across the propellant grain, which is attributed to the casting process [12].

From studying diffusion of nutrients and drugs in brain tissue [13] to the overall elasticity of structural materials [14], the macroscopic behavior is dependent on an accurate characterization of the microstructure. In the study of heterogeneous materials, which is the physical application considered in this work, much effort has been dedicated to developing theories that predict macroscopic behavior, e.g., effective material constants such as thermal conductivity, elastic moduli, and fluid permeability, based on knowledge of the microstructure. However, careful consideration of effective properties of noncrystalline microstructures that do not follow traditional microstructural assumptions such as statistical isotropy or alignment of inclusions has been limited. To overcome limitations of the morphological assumptions used in modeling randomly configured systems, microcomputer tomography (micro-CT) has become a popular method for obtaining a description of real microstructures including solid propellants [15,16], glass beads [17–20], and Fontainebleau sandstone [21], just to name a few. In particular, this paper applies tomographic characterization methods of polydisperse mixtures of ellipsoidal and spherical particles and develops microstructure-statistics-property relations (thermal conduction is explored in this paper) of real anisotropic material systems (when particles do not arrange isotropically or with ellipsoidal symmetry).

Particulate systems are often described by statistical characterization methods. Bernal [22] first motivated the importance of higher-order statistics using the radial distribution function to describe the structures of liquids. The significance of the statistical description has also been shown in several other fields of physics [23,24]. Frisch and Stillinger [25] introduced

---

[*]Corresponding author: kmatous@nd.edu

n-point probability functions, which are used in this work, to describe radiation scattering in packs of monodisperse spheres. While these statistical descriptors have been used for decades, accurately obtaining higher-order statistical information of real systems in three dimensions has proved difficult to this day. For example, Coker and Torquato [26] and Yeong and Torquato [27] computed two-point probability functions of a two-phase material, yet considered only two-dimensional slices and assumed rotational and translational invariance of the functions. Fullwood *et al.* [28] computed n-point probability functions of three-dimensional two-phase materials, but their computations were limited to relatively small systems. In our prior work [20], one-, two-, and three-point probability functions were calculated for a three-dimensional system of polydisperse spheres from micro-CT data. As multiphase polydisperse systems are considered in three dimensions, large packs must be used, resulting in even larger data sets.

Linking the morphology to the overall material response is a longstanding problem. In the material science community, the seminal multiscale techniques proposed by Hashin and Shtrikman [29], Willis [30], Bensoussan *et al.* [31], Hill [32], and Torquato [33] deserve attention, and many others have also contributed [34–39]. The work of Willis is of particular importance as it established a direct link between the statistical description and properties [30]. However, in [30] results were only obtained for simple morphologies with statistically isotropic or ellipsoidal symmetric statistics. This limitation is due to challenges in integrating complex integral kernels that are products of the second derivative of Green's function and two-point probability functions. In the work of Torquato and Sen [40], only statistically isotropic microstructures and those composed of aligned arbitrarily shaped inclusions were discussed. Among others, Ponte Castañeda [41] and Talbot and Willis [42] have proposed third-order models for nonlinear materials, yet once again only simple microstructures were considered due to the difficulty in obtaining real probability functions and integrating over them.

In order to accurately describe the microstructure, an image processing pipeline is presented to properly identify individual particles. State of the art in micro-CT analysis of highly packed particulate systems has been limited, to the best of our knowledge, to nearly monodisperse packs [17,19,43], and these works do not discuss in detail image processing steps. However, image processing steps can pollute predictions of physical properties. Following the identification of particles in the system through image processing, we present an algorithm that maps a voxel data set to a Euclidean, $\mathbb{R}^3$, representation (implemented in the SHAPE3D software package). A description in continuous Euclidean space simplifies analysis of such systems, reduces their data set size, improves their understanding, and aids in the development of new material formulations. Moreover, data set size reduction becomes increasingly important as more complicated systems are studied, and larger voxel data sets must be considered in order to resolve all important morphological features.

Next, we compute overall anisotropic properties of real granular mixtures without traditional assumptions on the complexity of the microstructure (statistically isotropic, aligned inclusions, etc.) using our PROP3D software package [44]. We show that for systems of polydisperse unaligned ellipsoidal inclusions, the importance of eliminating these assumptions is critical. The n-point probability functions are computed directly from three-dimensional micro-CT images using our statistical sampling code, STAT3D [20]. We show that the statistical functions of our polydisperse systems are not isotropic nor possess ellipsoidal or any other material symmetry. Thus closed-form solutions of overall properties are unachievable.

II. SAMPLE PREPARATION, MICRO-CT SCANNING, AND PARTICLE CHARACTERIZATION

This section describes methods to mix and pack polydisperse systems, to acquire data using micro-CT, to process data sets using image processing algorithms, and to model particles as ideal shapes. In this work, a surrogate system of rice grains and mustard seeds is used for their ellipsoidal and spherical shape, respectively. In our discussion, we label the mustard seeds as spheres due to their low eccentricities. However, all particles are modeled as ellipsoids.

A. Packing of polydisperse particulate mixtures

Packing methods presented here were developed and implemented to create homogeneous mixtures of particles with no long-range order while obtaining repeatable results. In order to satisfy these criteria, a manual packing procedure was developed similar to ones used in other works [19,45,46]. Note that packing in a more controlled environment, e.g., use of an electromechanical shaker as in [10,17,18,46], can produce more densely packed systems and could also be used as long as it satisfies criteria listed above. An important phenomenon to consider when creating these granular mixtures is segregation that can occur due to electrostatic effects and due to ease with which particles can roll. Moreover, the shape of the container and boundary effects were considered.

The first method is used for packing homogeneous polydisperse mixtures of ellipsoids and spheres while limiting boundary effects and segregation. Granular packs mixed using this method will be referred to as randomized packs. The container, as seen in Fig. 1, was designed to eliminate boundary effects and fill the entire viewing area within the micro-CT scanner. The container has a diameter of 62 mm and height of 65 mm, and hemispherical beads (3 mm radius) are attached to the boundary in order to minimize boundary effects. The randomized packs are prepared in the following steps: (I) Amount of each constituent (e.g., spheres, ellipsoids, etc.) is weighed with a high precision scale with 0.001 g accuracy. (II) Constituents are mixed together in a large bowl through manual stirring. (III) Mixture is poured into scanning container. (IV) Scanning container is manually shaken vigorously in all directions. (V) Container is tapped gently (manually) to allow particles to settle. This tapping is done on a leveled laboratory table until the observed level of particles (height) in the container stops descending. Let us note that steps (II) and (IV) are repeated until the mixtures are visually homogeneous. The vigorous manual shaking [step (IV)] is essential for eliminating segregation. Note that the gentle tapping and rough container walls were motivated by packing procedures reported in the work of Aste *et al.* [19].

FIG. 1. (Color online) Scanning container filled with 50% weight of spheres to ellipsoids. The hemispherical beads (3 mm radius) on the boundary of the container are used to minimize boundary effects. The container is 65 mm in height and 62 mm in diameter.

The second method was developed to pack random homogeneous systems of particles with an increased amount of anisotropy. Granular packs created with this method are referred to as semiordered packs as particles have a stronger probability of aligning. Note that this method is only used to create packs of ellipsoidal particles, and thus segregation is not an issue. To prepare semiordered packs of aligned particles, a sequential addition procedure with manual shaking, as introduced by Baker and Kudroli [46], is implemented. The same sized cylindrical container was used, but no hemispherical beads were attached to the boundary of the container in order to prevent the irregular boundary from randomizing the sample. The semiordered packs are prepared in the following steps. (I) A thin layer of particles is poured into container. (II) On a leveled laboratory table, the container is oscillated manually back and forth 20 times in the same direction. (III) Container is tapped gently five times. These steps are applied to thin layers so that the particles on top of the pack can move freely. We repeat these steps until the container is full. Oscillating the container in the same direction allows particles to align, and manual tapping is again done to allow the particles to settle.

B. Data set acquisition

Once packs are prepared, all samples are scanned using a Skyscan 1172 micro-CT machine. This particular scanner has the ability to produce data sets that capture features that are ∼0.7 μm. A convergence study was done on a pack of polydisperse spheres to show that the particle volume fraction of a sample is maintained for resolutions of 69.4, 34.7, 17.4, and 8.7 μm per pixel. The standard deviation in volume fraction for all of these scans was 0.0055, which is less than 1% of the mean volume fraction. A resolution of 69.4 μm per pixel was selected for all compositions described in this work.
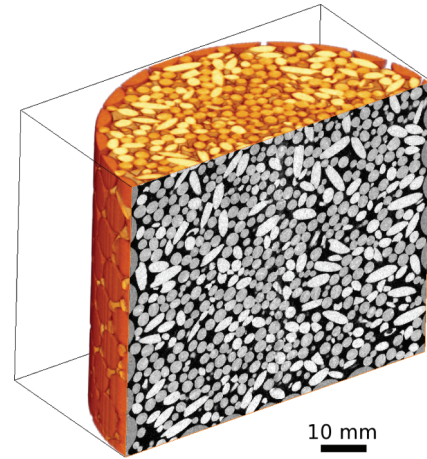

FIG. 2. (Color online) Surrogate system of ellipsoids and spheres with 50% weight fraction of constituents. Observe the hemispherical beads at the boundary that are used to randomize the packs and limit boundary effects. The brightest particles correspond to the ellipsoidal particles, while the darker ones correspond to spherical ones.

All data sets are on the order of 10^8 voxels (voxel = 3D pixel). The average diameter of the spherical particles, the smallest sized inclusion in our mixtures, is ∼2 mm. With a resolution of 69.4 μm, this is ∼30 voxels in diameter, which is a good resolution for the statistical characterization that follows.

The three-dimensional voxel data set of the 50% weight fraction of spherical to ellipsoidal particles is shown in Fig. 2. This data set will be used to describe steps for characterizing the microstructure. This cylindrical data set has a diameter of $D = 57.67$ mm (831 pixels) and a height of $H = 48.51$ mm (699 pixels), which corresponds to 3.79×10^8 voxels.

C. Image processing

Once the three-dimensional voxel data set is obtained, image processing algorithms are used to identify particles, and these voxel particles are then modeled as idealized shapes. The purpose of characterizing particles as idealized shapes is to understand the influence of different particle types on the macroscopic behavior and to provide a description of the microstructure in continuous Euclidean space, $\mathbb{R}^3$. This compact representation can be beneficial for design of new material formulations, for example. Image processing routines for identifying particles in a voxel data set are well established [47]. For a system of convex-shaped objects with no hollow regions, a typical image processing pipeline is to eliminate noise in the data set by using an edge-preserving smoothing algorithm, to identify the particulate material by thresholding, and to segment the data set such that individual particles are represented by connected groups of voxels. Two common segmentation algorithms are watershed-based segmentation and the opening algorithm (erosion followed by dilation). Unfortunately, a watershed-based algorithm is limited as it only properly separates data sets of convex-shaped objects, while the opening algorithm distorts shapes for nonspherical objects. For polydisperse systems with nonconvex features, which is common for real materials, these standard image processing steps will result in improperly segmented data
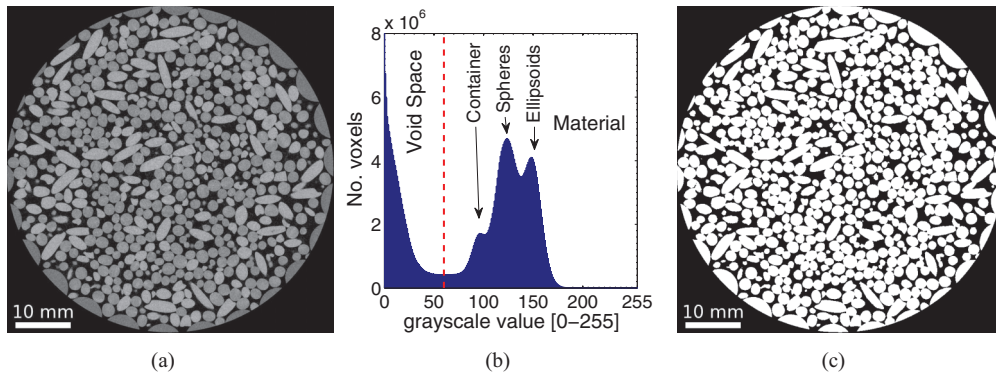
FIG. 3. (Color online) Illustration of image processing steps (i)–(iii). (a) Gray scale image after applying smoothing algorithm. (b) Distribution of voxel gray scale values. The dashed line indicates the cutoff value between material and void space. (c) Image slice after thresholding and filling voids within particles.

sets [47]. Because the particles of our surrogate system have internal voids and nonconvex surfaces, this traditional processing pipeline requires enhancement to accurately capture the microstructure. Note that in general all segmentation algorithms lead to some volume removal.

In order to limit and control the errors in the image processing pipeline, we propose a strategy based on interplay between voxel analysis and analysis in $\mathbb{R}^3$. The following image processing steps were developed using Visage Imaging Inc.'s *Amira* [48] in conjunction with Skyscan's *CTAn* [49] and the SHAPE3D software developed in this work. (i) The voxel data set is smoothed using the Kuwahara edge-preserving median filter algorithm [50] in order to eliminate noise. A resulting two-dimensional slice of the data set after smoothing is presented in Fig. 3(a). (ii) The particulate phases are thresholded based on the gray scale distribution of particles [Fig. 3(b)]. In this distribution, the three peaks on the right are related to the average gray scale values of the ellipsoids, spheres, and the container, and the left peak is considered void space. The threshold cutoff (red dashed line), which distinguishes between void space and material, is chosen to be the local minimum value between the two leftmost peaks and is 60 for this data set. (iii) Voids within the particles are filled. The resulting data set slice after this step is presented in Fig. 3(c). Notice how many of these particles are joined. (iv) A watershed segmentation algorithm is used to separate individual particles. (v) To eliminate boundary effects due to the hemispherical beads that are fixed to the scanning container, a volume of interest (VOI) is defined. The VOI [the circular blue region in Fig. 4(a)] is chosen such that the boundary effects on the statistical characteristics are minimized or eliminated. The VOI is determined by decreasing the cylindrical volume's diameter and height by increments of 10 voxels until the particle volume fraction saturates to within 1%. The resulting VOI has a diameter of $D_{VOI} = 46.57$ mm and a height of $H_{VOI} = 37.4$ mm (63.70 cm^3). (vi) Geometric quantities of individual particles including volume, surface area, moments of inertia, the mean gray scale value and centroid coordinates are computed. (vii) It is determined which particles are still connected due to the inefficiency of the segmentation algorithm, and these particles are marked [Fig. 4(b)]. To determine which particles were not separated

in step (iv), one can analyze certain geometric quantities of the voxel particles to see if they match the parameters of the shapes expected in the sample, i.e., if some voxel particles are larger than the known distribution of particles, they should be segmented further. Because this system is composed of particles closely resembling ellipsoids, a voxel particle not matching an ellipsoid is marked for additional image segmentation steps. The method for modeling a voxel particle as an ellipsoid is described in Sec. II D. (viii) A combination of the opening algorithm with watershed segmentation is used to separate the marked particles identified in step (vii) using SHAPE3D (see Sec. II D). (ix) For newly separated particles, geometric quantities are computed. (x) The phase of each particle is determined based on the mean gray scale value. The average gray scale value of each particle is described in Figs. 5(a) and 5(b), where d is the representative sphere diameter computed as $d = \sqrt[3]{6V_{ct}/\pi}$ and V_{ct} is the volume of the voxel particle. Here and in what follows pdf is used as an abbreviation for the probability density function. Considering the local minimum in Fig. 5(a) and the distribution of particle sizes in Fig. 5(b), the average gray scale cutoff value for the 50% weight fraction of spheres is 136.
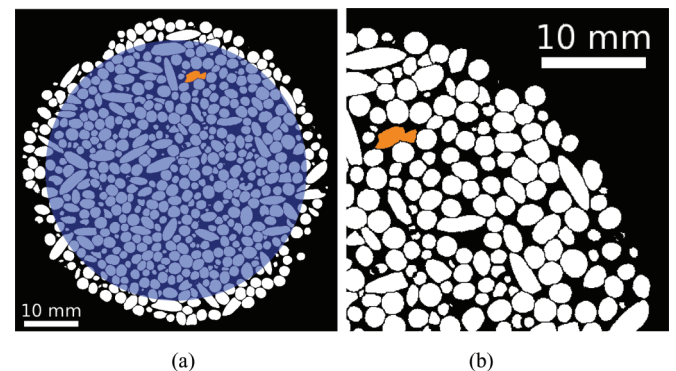

FIG. 4. (Color online) Illustration of image processing steps (iv)–(vii). (a) A data set slice after image segmentation in step (iv). The shaded circular section indicates the volume of interest (VOI). (b) A section of (a) that illustrates particles remaining connected after step (vi) (filled particle).
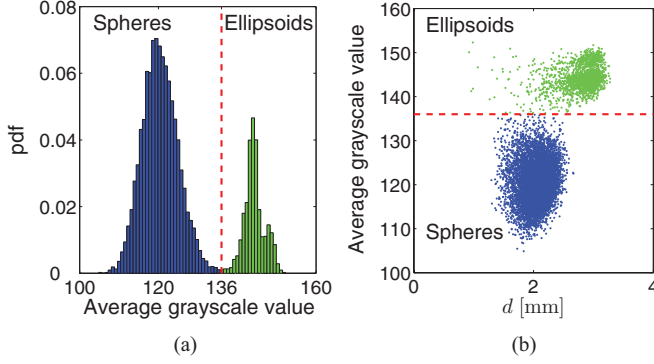
FIG. 5. (Color online) Illustration of image processing step (x). (a) Distribution of mean gray scale value for particles in the system depicted in Fig. 2. (b) Scatter plot of particle size, d, versus mean gray scale value. The red dashed line in (a) and (b) indicates the average gray scale cutoff value.

Figure 6 shows the resulting data set after image processing, where the spherical and ellipsoidal particles are colored blue (dark gray) and green (light gray), respectively. Packs of voxel particles will be referred to as voxel packs. An error measure is introduced to quantify the volume loss due to the image segmentation steps,

$$0 \leqslant \varepsilon_{IP} = \frac{\left| c_p^{v,B} - c_p^{v,A} \right|}{c_p^{v,B}} \times 100 \leqslant 100[\%], \qquad (1)$$

where $c_p^{v,B}$ and $c_p^{v,A}$ are the total particle volume fractions of a voxel pack before and after image segmentation steps, respectively. For the 50% weight spherical particle pack, $c_p^{v,B} = 0.6770$ and $c_p^{v,A} = 0.6594$, which represents a volume loss of $\varepsilon_{IP} = 2.60\%$ as a result of the image segmentation algorithms used. Note that respective phases (mustard and rice) can only be identified after all image segmentation steps, and c_e^v and c_s^v will refer to the volume fractions of ellipsoids and spheres in the voxel pack ($c_p^{v,A} = c_e^v + c_s^v$), respectively. For this pack, $c_e^v = 0.2701$ and $c_s^v = 0.3893$. Relevant information including the volume fractions and other morphological characteristics of all mixtures studied are presented in Tables I and II.
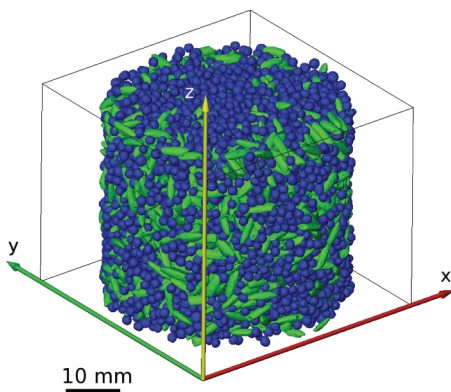

FIG. 6. (Color online) Voxel pack of 50% weight of constituent mixture. A voxel pack is the voxel data set after image processing. The spherical and ellipsoidal particles are colored blue (dark gray) and green (light gray), respectively.

TABLE I. Description of randomized packs, where W is the weight of each particulate phase (e or s), and D and H are the diameter and height, respectively, of the data set or VOI. ε_{IP} denotes the volume error due to image segmentation. The subscripts e and s refer to the ellipsoidal and spherical particulate constituents, respectively.

Pack [wt %]	0	25	50	75	100
W_e [g]	100.001	74.998	50.003	25.007	0.000
W_s [g]	0.000	24.997	50.003	75.002	100.000
D [mm]			—————— 57.67 ——————		-
D_{VOI} [mm]			—————— 46.57 ——————		-
		Higher volume fraction packs			
H [mm]	41.43	42.74	48.51	50.04	51.42
H_{VOI} [mm]	30.33	31.64	37.41	38.93	40.32
ε_{IP} [%]	2.23	2.85	2.60	2.72	3.66
		Lower volume fraction packs			
H [mm]	41.22	43.10	46.22	49.62	49.76
H_{VOI} [mm]	30.12	31.99	35.12	38.52	38.66
ε_{IP} [%]	2.22	2.72	2.46	2.66	3.52

D. Modeling voxel pack as pack of idealized shapes

Taking into consideration knowledge about the microstructure, all voxel particles are modeled as ellipsoids in $\mathbb{R}^3$. Voxel particles are fitted to idealized shapes by optimizing two fitness functions that best characterize a particle's volume, surface area, and orientation. The first function minimized is

$$\Pi_1(k) = \omega \frac{|k^3 V_{pa} - V_{ct}|}{|V_{ct}|} + (1 - \omega) \frac{|k^2 S_{pa} - S_{ct}|}{|S_{ct}|}, \qquad (2)$$

where V_{ct} and S_{ct} are the volume and surface area calculated for a particle in the voxel pack, V_{pa} and S_{pa} are the volume and surface area of the ideal shape being optimized, and ω is a weight factor between a particle's volume to surface area. The weight factor was chosen to be $\omega = 0.8$ in our work. The

TABLE II. Summary of volume, ΔV, surface area, ΔS, and orientation, $\Delta \Pi_2$, errors between voxel particles and ellipsoids. The unit of all values is %. Less than 0.1% of all particles considered in these mixtures have $\Delta \Pi_2 > 5\%$, and less than 14.3% of all particles have $\Delta S > 5\%$.

| Pack [wt %]	0	25	50	75	100
		Higher volume fraction packs			
ΔV (mean)	0.65	0.50	0.41	0.33	0.41
ΔV (max)	3.63	3.29	3.29	3.27	3.69
ΔS (mean)	4.11	3.16	2.56	2.03	2.62
ΔS (max)	34.22	28.55	28.62	28.15	35.28
$\Delta \Pi_2$ (mean)	1.09	0.56	0.38	0.22	0.21
$\Delta \Pi_2$ (max)	14.17	8.41	8.37	5.68	18.69
		Lower volume fraction packs			
ΔV (mean)	0.63	0.52	0.35	0.32	0.40
ΔV (max)	3.69	3.52	3.50	3.22	3.54
ΔS (mean)	3.99	3.31	2.17	2.04	2.50
ΔS (max)	35.81	32.26	26.05	27.56	32.71
$\Delta \Pi_2$ (mean)	1.05	0.57	0.36	0.22	0.21
$\Delta \Pi_2$ (max)	6.47	12.79	11.43	4.97	10.09
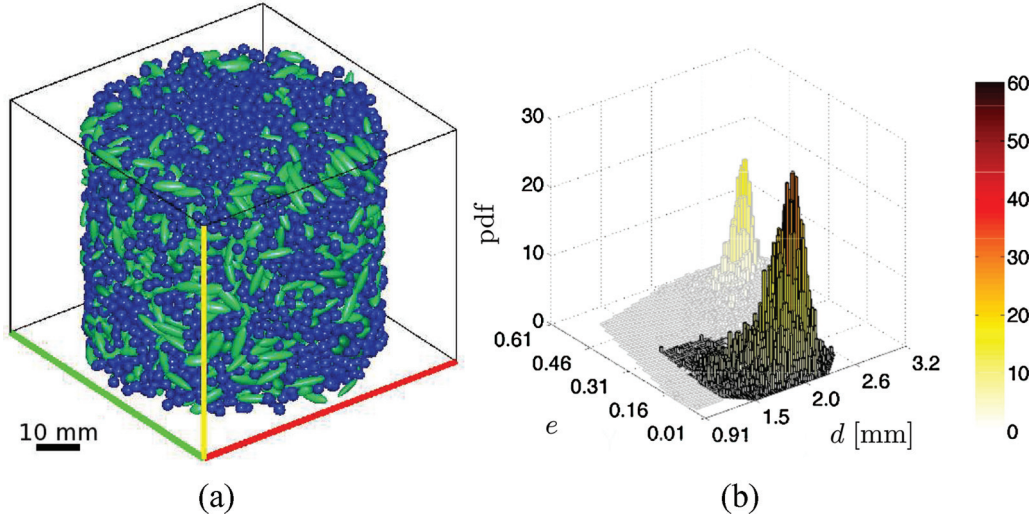
FIG. 7. (Color online) (a) Idealized pack of 50% weight of constituent mixture. There are 2276 ellipsoidal and 8344 spherical particles in this granular pack. Comparing Figs. 6 and 7(a) shows qualitatively that the idealized pack in Euclidean $\mathbb{R}^3$ space is an accurate representation of the voxel pack. (b) Particle distribution of voxel pack from Fig. 6. d is the representative sphere diameter and e [Eq. (6)] is the measure of eccentricity.

scaling factor k determines the scale of the final semiaxes as

$$\begin{pmatrix} a \\ b \\ c \end{pmatrix} = k \begin{pmatrix} a^* \\ b^* \\ c^* \end{pmatrix}, \tag{3}$$

where a, b, and c are the final semiaxes lengths of the ideal shape with $a > b > c$. The semiaxes lengths a^*, b^*, and c^* are computed from the inertia tensor of the voxel particle, $\boldsymbol{I}_{ct}$, assuming that the particle is an ellipsoid. The use of a scaling factor k ensures that the ratios between a^*, b^*, and c^* and a, b, and c are preserved so that the idealized particle better mimics the overall shape.

A second fitness function, $\Pi_2(\alpha,\beta,\gamma)$, is defined to adjust the orientation of the idealized shape to best mimic the voxel particle as

$$\Pi_2(\alpha,\beta,\gamma) = \frac{\|\boldsymbol{R}(\alpha,\beta,\gamma)\boldsymbol{I}_{pa}\boldsymbol{R}(\alpha,\beta,\gamma)^{-1} - \boldsymbol{I}_{ct}\|_{\mathbb{F}}}{\|\mathbf{I}_{ct}\|_{\mathbb{F}}}, \tag{4}$$

where $\boldsymbol{I}_{pa}$ is the inertia tensor of the ideal shape that is being optimized. α, β, and γ are angles by which the orthogonal rotation matrix $\mathbf{R}$ adjusts $\boldsymbol{I}_{pa}$. Also, $\boldsymbol{A} = \boldsymbol{R}\boldsymbol{A}^*\boldsymbol{R}^{-1} = [\boldsymbol{\eta}_1,\boldsymbol{\eta}_2,\boldsymbol{\eta}_3]^T$ gives the final orientation vectors $\boldsymbol{\eta}_1$, $\boldsymbol{\eta}_2$, and $\boldsymbol{\eta}_3$ that correspond to the directions of a, b, and c, respectively. Here, $\|\bullet\|_{\mathbb{F}}$ represents the Frobenius norm. Note that we place the ellipsoid's origin at the centroid (X_c,Y_c,Z_c) of the voxel object, and the density of all particles is assumed constant in this step.

The resulting errors between voxel and ideal particles are considered by looking at differences in the volume, surface area, and inertia tensors after optimizing the objective functions. The first metric, ΔV, quantifies the difference in volume (as a percentage) between a voxel particle and its corresponding ellipsoid:

$$0 \leqslant \Delta V = \frac{|V_{pa} - V_{ct}|}{|V_{ct}|} \times 100 \leqslant 100[\%]. \tag{5}$$

The second metric, ΔS, quantifies the difference in surface area (as a percentage) in the same manner as ΔV [see Eq. (5)]. The third metric, $\Delta\Pi_2 = \Pi_2 \times 100[\%]$, quantifies differences in orientation. Particles with $\Delta\Pi_2 > 5\%$ are marked in image processing step (vii) for additional segmentation in step (viii) [see orange (gray) particle in Fig. 4 and description in Sec. II C].

The corresponding idealized pack and distribution of particles for the voxel pack are presented in Fig. 7, where e is a measure of eccentricity defined as

$$e = \frac{1}{3}\left(\frac{\sqrt{a^{*2} - b^{*2}}}{a^*} + \frac{\sqrt{b^{*2} - c^{*2}}}{b^*} + \frac{\sqrt{a^{2*} - c^{*2}}}{a^*} \right). \tag{6}$$

Higher values of e correspond to more eccentric particles, and a perfect sphere corresponds to $e = 0$. The distribution outlined in black corresponds to the spheres [blue (dark gray) particles], while the distribution outlined in gray corresponds to ellipsoids [green (light gray) particles]. As can be seen in Fig. 7, the average eccentricity of the mustard seeds is small. Thus they are referred to as spherical. Note that a substantial reduction of the data set size from $\sim 3.79 \times 10^8$ voxels to 10 620 ellipsoids was achieved. Considering that an ellipsoid is described by its centroid (X_c,Y_c,Z_c), semiaxes lengths (a,b,c), and three angles (α, β, and γ), we need nine numbers to characterize an ellipsoidal particle. Thus 95 580 numbers are needed to describe this pack. Compared to the 3.79×10^8 voxels, this data set is compressed by approximately 4000 times.

The distributions of errors in volume, surface area, and inertia tensor for all particles in the pack are shown in Fig. 8. All average errors are below 3%. Note that the maximum error in surface area, ΔS, is large relative to ΔV, because the weight factor, ω, favors matching the volume of the particle over the surface area. Furthermore, it is well known that the voxel representation of a surface is inaccurate and cannot be improved by increasing the voxel resolution [51]. Capturing the surface area of a voxel object accurately is nontrivial and requires fitting
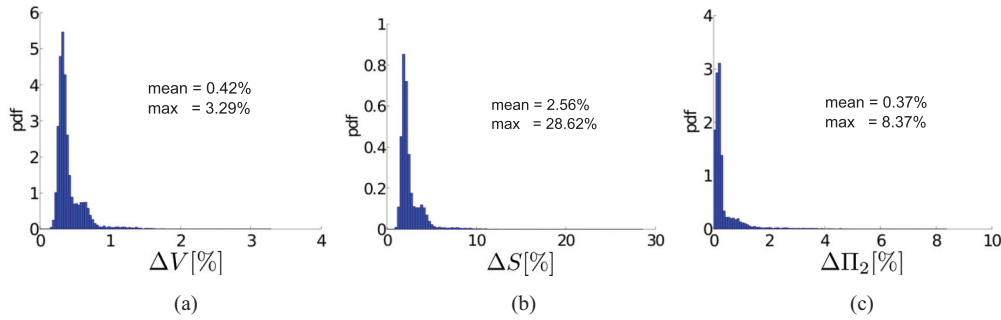
FIG. 8. (Color online) Distributions of errors in modeling voxel particles as ellipsoids for 50% weight mixture shown in Figs. 6 (voxel pack) and 7(a) (idealized pack). (a) Distribution of the particles' errors in volume, ΔV. (b) Distribution of the particles' errors in surface area, ΔS. (c) Distributions of particles' errors in inertia tensors, $\Delta \Pi_2$.

a smooth surface to a stepwise boundary [51,52]. Because a sophisticated surface representation was not considered in this work, ω was chosen to be 0.8. Nevertheless, only 3.99% of particles in this pack have $\Delta S > 5\%$. In addition, note that while Π_2 is used to optimize the orientation of the idealized shape, this value is also a measure of how well an idealized shape fits a voxel particle in an overall sense. For this pack, only 0.03% of particles have orientation errors of $\Delta \Pi_2 > 5\%$. Note that using a traditional watershed-based segmentation algorithm without our $\mathbb{R}^3$ mapping [system before step (vii)] would result in $\Delta \Pi_2(\max) = 16.04\%$, and 0.34% of particles having $\Delta \Pi_2 > 5\%$. This shows that a substantial improvement was achieved [$\Delta \Pi_2(\max)$ was improved $2\times$ and $\Delta \Pi_2 > 5\%$ was improved $10\times$].

E. Pack analysis

Using the microstructure characterization procedures described above, five randomized compositions and one semiordered pack of ellipsoids are characterized. These data sets provide a foundational data set for analyzing the microstructure's effect on overall material properties that will be presented in Sec. V.

1. Semiordered pack of ellipsoids

The voxel pack representation after image processing with the associated distribution of particles is presented in Fig. 9,

where the size of the cylindrical domain has a diameter of $D = 59.44$ mm and a height of $H = 47.16$ mm. This pack had a particle volume fraction of $c_p^{v,B} = 0.6841$ before particle segmentation and was reduced to $c_p^{v,A} = 0.6655$ after image segmentation steps, corresponding to a volume loss of $\varepsilon_{IP} = 2.71\%$. The VOI for this sample is $D_{\mathrm{VOI}} = 45.24$ mm and $H_{\mathrm{VOI}} = 33.03$ mm. When modeling the voxel particles as ellipsoids, the mean errors of ΔV, ΔS, and $\Delta \Pi_2$ are 0.70%, 4.48%, and 2.20%, respectively. The maximum errors in ΔV, ΔS, and $\Delta \Pi_2$ are 2.69%, 20.98%, and 11.65%, and 24.91% and 0.69% of all particles have $\Delta S > 5\%$ and $\Delta \Pi_2 > 5\%$.

In Fig. 9(a), it can be seen that particles are aligned in the y direction. The orientation of an ellipsoidal particle is described by two angles with respect to the basis vector of the longest semiaxis, $\boldsymbol{\eta}_1$: the azimuthal angle (projected orientation onto the xy plane) and the altitude angle (with respect to the z axis). These angles are referred to as θ_a and ϕ_a (see Fig. 10) and are found from the orientation of an idealized shape. The distributions of the azimuthal and altitude angles for the semiordered pack are presented in Fig. 11. The distribution of ϕ_a shows that ellipsoids are more likely to lie horizontally ($\phi_a = 0°$) than in the unstable vertical position ($\phi_a = 90°$), while the distribution of θ_a shows that ellipsoids are preferentially aligned in the y direction ($\theta_a = -90° = 90°$), which can also be observed in Fig. 9(a). This anisotropic morphology has a critical impact on the overall thermal-conductivity estimates presented in Sec. V.
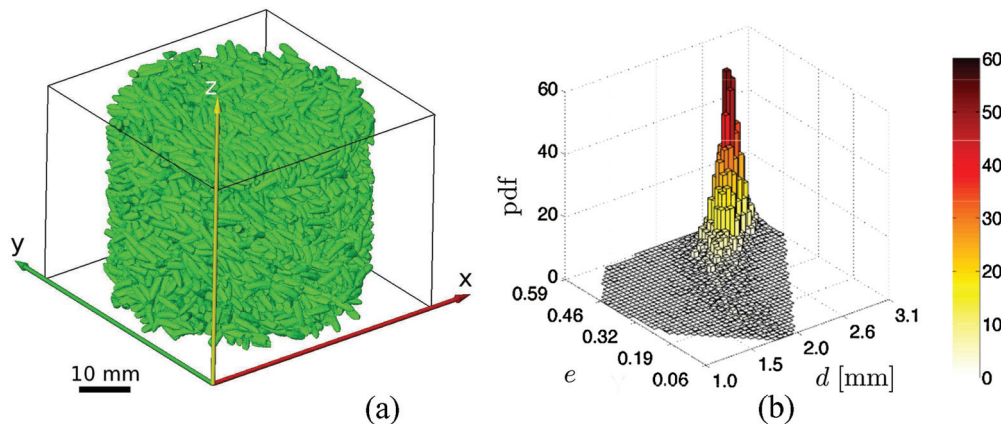

FIG. 9. (Color online) (a) Voxel pack of semiordered sample. There are 6536 ellipsoidal particles in this pack. (b) Distribution of particles for semiordered voxel pack shown in (a). d is the representative sphere diameter and e [Eq. (6)] is the measure of eccentricity.
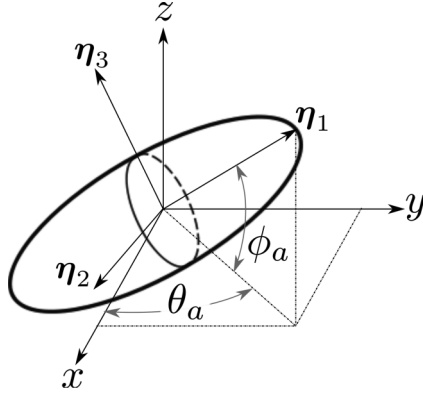
FIG. 10. Definition of ellipsoid's orientation in Cartesian coordinate system with respect to the largest semiaxis, $\boldsymbol{\eta}_1$. ϕ_a is a particle's elevation angle and θ_z is a particle's azimuthal angle, θ_a.

2. Randomized mixtures

Five compositions at 0%, 25%, 50%, 75%, and 100% weight of spheres to ellipsoids are considered. These five compositions are created by weighing an appropriate amount of each constituent and are then packed and tomographically characterized two times to confirm the repeatability of the steps described in this section (we refer to these two scans as higher and lower volume fraction packs depending on their packing density). Table I shows information about each voxel pack including the weight of each constituent, sizes of the data sets, and the error introduced in the image segmentation steps. The largest volume losses, ε_{IP}, occur for the spherical particle packs. However, all volume losses are less than 3.66%. Note that the height of the volume analyzed, H, increases with increasing wt % of spherical particles, because the spherical particles are less dense than the ellipsoidal ones. This can be also observed in Fig. 2, since darker gray corresponds to less dense material. The resulting volume fractions of all randomized compositions before and after image segmentation, $c_p^{v,B}$ and $c_p^{v,A}$, are presented in Fig. 12(a). Figure 12(b) shows the volume fraction of each constituent for the corresponding composition. In these two figures, the two samples for each composition are represented by two data points, and the lines are the means. All differences in the total

particle volume fractions after segmentation, between the two packs of each composition analyzed (higher and lower volume fraction packs), are below 0.008 [maximum difference is for 25% mixture; see Fig. 12(a)]. The maximum differences between the phase volume fractions, c_e^v and c_s^v, are 0.0191 and 0.0156, respectively, for the 50% mixture [see Fig. 12(b)]. Recall that $c_p^{v,A} = c_e^v + c_s^v$. As the particle volume fractions, $c_p^{v,B}$, can theoretically be in the range [0,1], these differences between the two data points at each composition are small. The number of particles per volume is plotted for each of the packs in Fig. 13, where N_p is the number of particles in the VOI. The number of total particles increases with increasing wt % of spherical particles, because the volume of a spherical particle is smaller than the volume of an ellipsoidal particle as evident in the distribution of particles for the 50% pack in Fig. 7(b). The mean and max errors between voxel particles and their corresponding ideal ellipsoidal representation are presented in Table II. All mean errors for each pack are below 5%. As discussed earlier, noticeable maximum errors in the surface area are related to errors in representing the surface of voxel particles. Moreover, noticeable maximum errors for Π_2 exist for a small number of particles that do not match an ellipsoid well. Overall, the low errors achieved throughout the microstructure characterization process show that sample preparation, data acquisition, and image processing steps produce scientifically sound and repeatable results with well controlled errors.

The mixture of randomized ellipsoids (0 wt % spherical particles) has a volume fraction consistent with packing simulations of monodisperse ellipsoids reaching a maximally random jammed state [53]. For the average size ellipsoidal particle ($a = 3.04$ mm, $b = 1.11$ mm, and $c = 0.83$ mm), a maximum packing volume fraction can be extrapolated to be 0.68 from the work of Chaikin *et al.* [53] ($c_p^{v,B} = 0.66$ in this work). It is expected that this volume fraction should be similar as the ellipsoidal particles have a small range in size as seen in Fig. 7. The volume fraction of maximally jammed monodisperse spheres in the work of Chaikin *et al.* [53] is 0.64, and the volume fractions for the compositions with 100% spheres considered in this work is higher ($c_p^{v,B} = 0.70$ from Fig. 12) due to the polydispersity as evidenced by the range in sizes in Fig. 7 (distribution outlined in black). Note that this volume fraction falls below 0.74, the assumed maximum achievable volume fraction of monodisperse spheres first proposed by Keplar and supported by many thereafter [54]. When considering all of the randomized compositions, there is an increasing trend in volume fraction, c_p^v. It is known that when the scales of two inclusions are significantly different, the mixtures will have higher volume fractions than the maximum volume fractions of a single constituent for monomodal spheres [55]. However, as the smallest semiaxes of the ellipsoids are similar to the average radius of the spherical particles, no such effect is observed.

The distributions of particle orientations for the randomized pack with 100% weight of ellipsoids is shown in Fig. 14. Notice that there is no preference of the randomized pack's ellipsoids azimuthal angle, θ_a (compare with Fig. 11 for semiordered pack). Moreover, there is a low probability that particles are suspended in the unstable vertical position, $\phi_a = 0°$. This randomness in the azimuthal angle, θ_a, confirms the
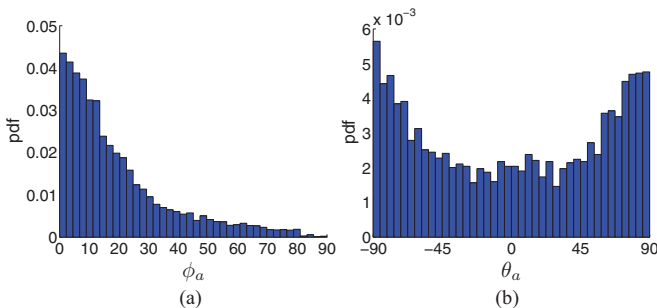

FIG. 11. (Color online) (a) Distribution of particles' elevation angles, ϕ_a, for semiordered pack shown in Fig. 9(a). (b) Distribution of particles' azimuthal angles, θ_z, for semiordered pack shown in Fig. 9(a).
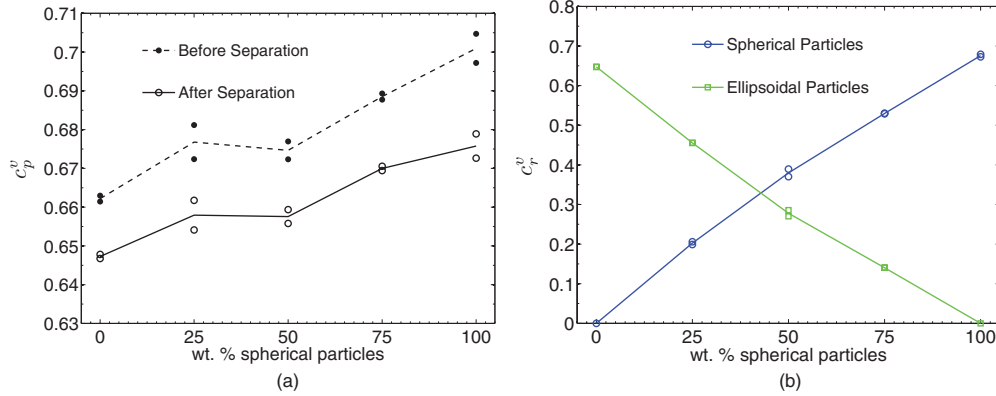
FIG. 12. (Color online) (a) Volume fractions, c_p^v, before and after image segmentation of randomized compositions described in Table I. Note that two samples for each composition were studied and are referred to as higher volume fraction packs (top points) and lower volume fraction packs (bottom points). (b) Volume fractions of each constituent, c_r^v, for segmented data sets in (a) after segmentation (empty circles).

randomizing effects in the sample preparation steps. The ellipsoidal particles in the other randomized packs exhibit similar trends in their orientations and are not reported here.

When comparing the semiordered pack of ellipsoids to the randomized one, the volume fraction of the semiordered ellipsoid pack is higher. This is in agreement with studies of ordered packs of monodisperse ellipsoids, as they are known to have a maximum particle volume fraction of 0.74–0.77 [56]. When comparing the altitude angle, ϕ_a, distributions between the semiordered and randomized pack, there is a higher probability of the semiordered pack particles existing in the xy plane ($\phi_a = 0°$) and a preferred direction for θ_a (see Figs. 11 and 14).

Let us note that the microstructure characterization method presented in this work can be used in a variety of applications as well as in validation of packing simulations [57,58]. In this work, the data sets provide a foundational set for considering the microstructure's effect on overall properties, and the effect of these packing configurations on the overall anisotropic thermal-conductivity tensor will be explored in the remainder of this paper.
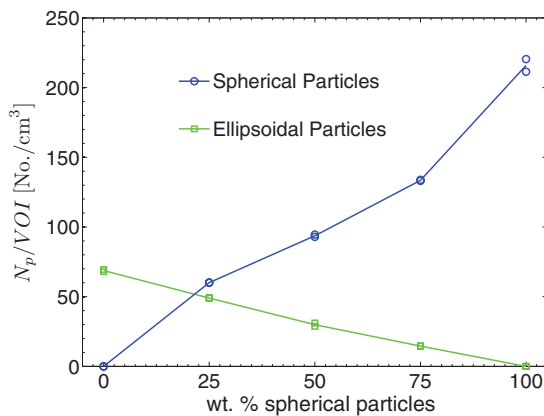
III. THEORETICAL OVERVIEW OF OVERALL ANISOTROPIC PROPERTIES

Using the Hashin-Shtrikman variational principle and assuming that particulate composites are homogeneous and ergodic, Willis formulated a second-order approximation of bounds on elastic and conductivity constants in which the two-point probability functions are embedded within the mathematical formulation directly [30]. In Willis' work, assumptions about the configuration of the particles were made when computing overall properties. In this work, upper and lower anisotropic bounds as well as anisotropic self-consistent estimates are computed without assumptions of statistical isotropy nor ellipsoidal or any other material symmetry for complex tomographically characterized polydisperse microstructures. A simple overview of theory is discussed next.

A. *n*-point probability functions

As described in [20,44], the *n*-point probability functions are derived using a phase indicator function at a position $\boldsymbol{x}$ in a sample α of an ensemble space $\mathcal{E}$:

$$\chi_r(\boldsymbol{x};\alpha) = \begin{cases} 1 & \text{if } \boldsymbol{x} \text{ in phase } r, \\ 0 & \text{otherwise.} \end{cases} \quad (7)$$
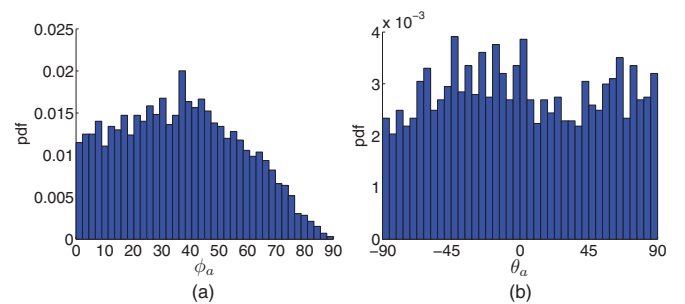

FIG. 14. (Color online) (a) Distribution of particles' elevation angles, ϕ_a, for the pack with 0% weight of spherical particles. (b) Distribution of particles' azimuthal angles, θ_z, for the pack with 0% weight of spherical particles.

FIG. 13. (Color online) Number of particles, N_p, per cm^3 as a function of the wt % of spherical particles for randomized compositions described in Table I and Fig. 12(b).

An ensemble is a collection of material samples being considered. The ensemble average is given by

$$\overline{\chi_r(\boldsymbol{x})} = \int_{\mathcal{E}} \chi_r(\boldsymbol{x}; \alpha) p(\alpha) d\alpha, \tag{8}$$

where $p(\alpha)$ is the probability density function of α in $\mathcal{E}$. The n-point probability function, $S_{r_1 r_2 \cdots r_n}(\boldsymbol{x}_1, \boldsymbol{x}_2, \dots, \boldsymbol{x}_n)$, is defined as

$$S_{rs \cdots q}(\boldsymbol{x}_1, \boldsymbol{x}_2, \dots, \boldsymbol{x}_n) = \overline{\chi_r(\boldsymbol{x}_1) \chi_s(\boldsymbol{x}_2) \cdots \chi_q(\boldsymbol{x}_n)}. \tag{9}$$

It represents the probability of phases $r, s, \dots, q$ existing at points $\boldsymbol{x}_1, \boldsymbol{x}_2, \dots, x_n$, simultaneously. In general, the probability functions for a heterogeneous material are spatially complex. In this work, a second-order model for computing bounds on overall anisotropic thermal conductivity is considered.

For statistical homogeneous materials, where the probability functions are translationally invariant, the one-point probability function attains a constant value, $S_r(\boldsymbol{x}) = c$, and the two-point function simplifies to $S_{rs}(\boldsymbol{x}, \boldsymbol{x}') = S_{rs}(\boldsymbol{x} - \boldsymbol{x}')$. For statistically homogeneous systems, it is meaningful to define volume averages. When assuming ergodicity of homogeneous systems, ensemble averaging is equivalent to volume averaging in the infinite volume limit,

$$S_{rs \cdots q}(\boldsymbol{x}_1, \boldsymbol{x}_2, \dots, \boldsymbol{x}_n) = \lim_{\Omega \to \infty} \frac{1}{\Omega} \int_{\Omega} \chi_r(\boldsymbol{x}_1 - \boldsymbol{l}) \chi_s(\boldsymbol{x}_2 - \boldsymbol{l})$$
$$\cdots \chi_q(\boldsymbol{x}_n - \boldsymbol{l}) d\Omega, \tag{10}$$

where $\boldsymbol{l}$ is a translation vector and Ω is the volume of the domain. For homogeneous and ergodic systems, the one-point probability function is equivalent to the volume fraction of phase r [$S_r(\boldsymbol{x}) = c_r$]. The two-point probability functions of a statistically homogeneous and isotropic system (rotationally and translationally invariant) are defined as $S_{rs}(\boldsymbol{x}, \boldsymbol{x}') = S_{rs}(|\boldsymbol{x} - \boldsymbol{x}'|)$, where the function only depends on the distance between two points. For homogeneous systems with no long-range order, we observe two limit cases in the pointwise sense of the two-point probability functions, which can be expressed as

$$S_{rs}(\boldsymbol{x} - \boldsymbol{x}') \to \begin{cases} c_r \delta_{rs} & \text{as } \boldsymbol{x} - \boldsymbol{x}' \to \boldsymbol{0}, \\ c_r c_s & \text{as } \boldsymbol{x} - \boldsymbol{x}' \to \infty, \end{cases} \tag{11}$$

where δ_{rs} is the Kronecker delta. More information on the n-point probability functions can be found in work by Torquato [2] and Beran [59]. In this work, statistically anisotropic systems are considered, and n-point probability functions are used when addressing the issues of material order.

B. Hashin-Shtrikman variational principle

The Hashin-Shtrikman variational principle is employed to obtain bounds on thermo-mechanical properties of an anisotropic material as described in [29,30]. It is assumed that the material follows a constitutive relation of $\boldsymbol{q} = \partial w(\boldsymbol{Q})/\partial \boldsymbol{Q}$, where $w(\boldsymbol{Q})$ is an energy density function, $\boldsymbol{q}$ is the heat flux vector, and $\boldsymbol{Q} = -\nabla T$ is the negative temperature gradient for a temperature T at a point $\boldsymbol{x}$. When the material obeys Fourier's law, $\boldsymbol{q} = \boldsymbol{\kappa} \cdot \boldsymbol{Q}$ (linear constitutive relation), the energy density function is defined as $w(\boldsymbol{Q}) = (\boldsymbol{Q} \cdot \boldsymbol{\kappa} \cdot \boldsymbol{Q})/2 \geqslant 0$, where $\boldsymbol{\kappa}$ is the symmetric positive semidefinite second-order thermal-conductivity tensor. This symmetric positive
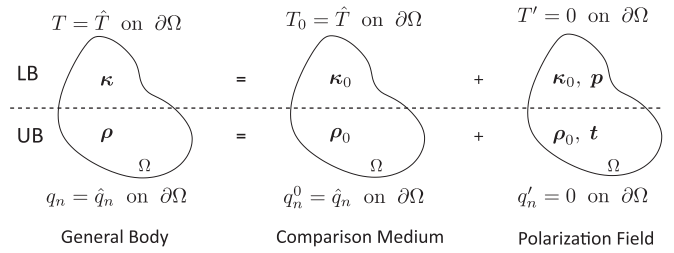

FIG. 15. Body decomposition with prescribed Dirichlet and Neumann boundary conditions, respectively, corresponding to the lower bound (LB) and upper bound (UB) formulations.

semidefiniteness requirement is in agreement with Onsager's reciprocity theorem [60]. Thus the generally anisotropic conductivity tensor computed in this work has six independent components. A complementary energy density, $w^*(\boldsymbol{q})$, can also be defined, where $w^*(\boldsymbol{q}) + w(\boldsymbol{Q}) = \boldsymbol{q} \cdot \boldsymbol{Q}$ and $\boldsymbol{Q} = \partial w^*(\boldsymbol{q})/\partial \boldsymbol{q}$. For a material following Fourier's law, $w^* = (\boldsymbol{q} \cdot \boldsymbol{\rho} \cdot \boldsymbol{q})/2 \geqslant 0$, where $\boldsymbol{\rho}$ represents the symmetric positive semidefinite second-order thermal-resistivity tensor. Note that at the continuum $\boldsymbol{\rho} = \boldsymbol{\kappa}^{-1}$. The internal energy and complementary internal energy of the system are defined as $E = \int_{\Omega} w \, d\Omega$ and $E^* = \int_{\Omega} w^* \, d\Omega$, respectively.

Hashin and Shtrikman [29] proposed the body decomposition, as shown in Fig. 15. The top half of this figure shows the body decomposition with a prescribed temperature field on the boundary, $\hat{T}$, which is used to compute the lower bound (LB) of the overall $\overline{\kappa}$. The bottom half of this figure shows the decomposition for a body with a prescribed normal heat flux, $\hat{q}_n$, and this formulation is used for computing the lower bound of the overall $\overline{\rho}$, corresponding to the upper bound (UB) of $\overline{\kappa}$. Note that quantities with $\bar{\bullet}$ denote an overall or volume averaged quantity, $\bar{\bullet} = 1/\Omega \int \bullet \, d\Omega$. The governing equations of these corresponding elliptic boundary-value problems are given by

$$\text{LB:}$$
$$\nabla \cdot [\boldsymbol{\kappa}_0 \cdot \boldsymbol{Q} + \boldsymbol{p}] = 0 \quad \text{in} \quad \Omega,$$
$$\boldsymbol{p} - [\boldsymbol{\kappa} - \boldsymbol{\kappa}_0] \cdot \boldsymbol{Q} = 0 \quad \text{in} \quad \Omega, \tag{12}$$
$$T' = 0 \quad \text{on} \quad \partial\Omega,$$

$$\text{UB:}$$
$$\nabla \cdot \boldsymbol{q} = 0 \quad \text{in} \quad \Omega,$$
$$\boldsymbol{t} - [\boldsymbol{\rho} - \boldsymbol{\rho}_0] \cdot \boldsymbol{q} = 0 \quad \text{in} \quad \Omega, \tag{13}$$
$$\boldsymbol{q}' \cdot \boldsymbol{n} = 0 \quad \text{on} \quad \partial\Omega,$$

where $\boldsymbol{\kappa}_0$ is the thermal-conductivity tensor of a comparison medium and $\boldsymbol{p}$ is the heat flux polarization tensor. T_0 and T' represent the homogeneous and fluctuation temperature fields, respectively. $\boldsymbol{q}'$ is the heat flux fluctuation field, $\boldsymbol{\rho}_0$ is the comparison medium resistivity tensor, $\boldsymbol{t}$ is the temperature gradient polarization field, $q_n = \boldsymbol{q} \cdot \boldsymbol{n}$ is the normal heat flux, and $\boldsymbol{n}$ is the unit normal vector. Note that this formulation is similar to theory for computing overall linear elastic constants [44].

Formulations equivalent to the ones described by the strong forms (12) and (13) can be obtained by minimizing the functionals,

LB:
$$2\mathcal{F}(\boldsymbol{p}) = \int_{\Omega}\left[\boldsymbol{p}\cdot[\boldsymbol{\kappa}-\boldsymbol{\kappa}_0]^{-1}\cdot\boldsymbol{p} + \boldsymbol{p}\cdot\int_{\Omega_{x'}}\boldsymbol{\Gamma}(\boldsymbol{x},\boldsymbol{x}')\right.$$
$$\left.\cdot[\boldsymbol{p}(\boldsymbol{x}')-\bar{\boldsymbol{p}}]d\Omega_{x'}-2\boldsymbol{p}\cdot\boldsymbol{Q}_0\right]d\Omega \quad (14)$$

and

UB:
$$2\mathcal{F}^*(\boldsymbol{t}) = \int_{\Omega}\left[\boldsymbol{t}\cdot[\boldsymbol{\rho}-\boldsymbol{\rho}_0]^{-1}\cdot\boldsymbol{t} + \boldsymbol{t}\cdot\int_{\Omega_{x'}}\boldsymbol{U}(\boldsymbol{x},\boldsymbol{x}')\right.$$
$$\left.\cdot[\boldsymbol{t}(\boldsymbol{x}')-\bar{\boldsymbol{t}}]d\Omega_{x'}-2\boldsymbol{t}\cdot\boldsymbol{q}_0\right]d\Omega, \quad (15)$$

for the lower and upper bound formulations, respectively. $\boldsymbol{\Gamma}(\boldsymbol{x},\boldsymbol{x}')$ is the second-order linear operator related to the Green's function solution. $\boldsymbol{Q}_0$ denotes the negative temperature gradient in a homogeneous comparison medium and $\boldsymbol{q}_0$ is the homogeneous heat flux. Note that the energy functional is defined as $\mathcal{F} = E_0 - E$, where E_0 is the internal energy of the comparison medium. $\mathcal{F}^* = E_o^* - E^*$, where E_0^* is the complementary internal energy of the comparison medium. For the upper bound formulation, $\boldsymbol{U}$ is the second-order linear operator related to the Green's function solution ($\boldsymbol{U} = \boldsymbol{\kappa} - \boldsymbol{\kappa}\cdot\boldsymbol{\Gamma}\cdot\boldsymbol{\kappa}$).

To find second-order estimates to the stationary point of Eqs. (14) and (15), trial fields of $\boldsymbol{p}$ and $\boldsymbol{t}$ are assumed piecewise constant in each phase r ($\boldsymbol{p}^* = \sum_{r=0}^n \chi_r \boldsymbol{p}_r$ and $\boldsymbol{t}^* = \sum_{r=0}^n \chi_r \boldsymbol{t}_r$ for a system of n particulate phases and a matrix corresponding to $r=0$). The following systems of algebraic equations are obtained after discretization of the polarization fields, $\boldsymbol{p}$ and $\boldsymbol{t}$, averaging over the ensemble space $\mathcal{E}$ and using the calculus of variations

LB:
$$c_r(\boldsymbol{\kappa}_r-\boldsymbol{\kappa}_0)^{-1}\cdot\boldsymbol{q}_r + \sum_{s=0}^n\int_{\Omega_{x'}}\boldsymbol{\Gamma}^\infty(\boldsymbol{x}-\boldsymbol{x}')[S_{rs}(\boldsymbol{x}-\boldsymbol{x}')-c_rc_s]$$
$$\cdot\boldsymbol{q}_s\,d\Omega_{x'}=-c_r\overline{\boldsymbol{Q}} \quad (16)$$

and

UB:
$$c_r(\boldsymbol{\rho}_r-\boldsymbol{\rho}_0)^{-1}\cdot\boldsymbol{t}_r + \sum_{s=0}^n\int_{\Omega_{x'}}\boldsymbol{U}^\infty(\boldsymbol{x}-\boldsymbol{x}')[S_{rs}(\boldsymbol{x}-\boldsymbol{x}')-c_rc_s]$$
$$\cdot\boldsymbol{t}_s\,d\Omega_{x'}=-c_r\overline{\boldsymbol{q}}. \quad (17)$$

Here c_r and c_s are the volume fractions of phase r and s, respectively, $\boldsymbol{\kappa}_r$ is the thermal-conductivity tensor of phase r, while $\overline{\boldsymbol{Q}}$ is the overall negative temperature gradient. $\boldsymbol{\Gamma}^\infty$ and $\boldsymbol{U}^\infty$ are related to the Green's function solution for an infinite body. For the upper bound formulation, $\boldsymbol{\rho}_r$ is the resistivity tensor of phase r, while $\bar{\boldsymbol{q}}$ is the overall heat flux.

These systems of equations are solved for the piecewise-constant fields, $\boldsymbol{p}_r$ and $\boldsymbol{t}_r$, to find the mean polarization fields, $\overline{\boldsymbol{p}} = \sum_{r=0}^n c_r \boldsymbol{p}_r$ and $\bar{\boldsymbol{t}} = \sum_{r=0}^n c_r \boldsymbol{t}_r$. The volume averaged

constitutive relations,

LB: UB:
$$\bar{\boldsymbol{q}} = \overline{\boldsymbol{\kappa}}\cdot\overline{\boldsymbol{Q}} = \overline{\boldsymbol{\kappa}}_0\cdot\overline{\boldsymbol{Q}}+\overline{\boldsymbol{p}}, \quad \overline{\boldsymbol{Q}} = \overline{\boldsymbol{\rho}}\cdot\bar{\boldsymbol{q}} = \overline{\boldsymbol{\rho}}_0\cdot\bar{\boldsymbol{q}}+\bar{\boldsymbol{t}}, \quad (18)$$

are used to calculate the overall $\overline{\boldsymbol{\kappa}}$ and $\overline{\boldsymbol{\rho}}$, respectively. When $\boldsymbol{\kappa}_r - \boldsymbol{\kappa}_0$ is the smallest positive semidefinite matrix for all phases r in the lower bound formulation, the resulting $\overline{\boldsymbol{\kappa}}$ is the second-order lower bound of the conductivity tensor. Meanwhile, when $\boldsymbol{\rho}_r - \boldsymbol{\rho}_0$ is the smallest positive semidefinite matrix for all phases r in the upper bound formulation, the second-order lower bound of the resistivity tensor is obtained (upper bound of the conductivity tensor, $\overline{\boldsymbol{\kappa}} = \overline{\boldsymbol{\rho}}^{-1}$).

Another widely used model for computing overall material properties is the self-consistent estimate (SC). As described in Willis' work [30], self-consistent estimates are calculated by minimizing the volume averaged energy and complementary energy functionals $|\overline{\mathcal{F}}| = |E_0 - \overline{E}|$ and $|\overline{\mathcal{F}}^*| = |E_0^* - \overline{E}^*|$. This leads to $\overline{E} = E_0$ ($\overline{\boldsymbol{\kappa}} = \boldsymbol{\kappa}_0$) and $\overline{E}^* = E_0^*$ ($\overline{\boldsymbol{\rho}} = \boldsymbol{\rho}_0$). With this in mind, the following objective functions are minimized in order to compute self-consistent estimates,

SC-L: SC-U:
$$\Pi_{SC}^L = \|\boldsymbol{\kappa}_0 - \overline{\boldsymbol{\kappa}}\|_{\mathbb{F}} \quad \Pi_{SC}^U = \|\boldsymbol{\rho}_0 - \overline{\boldsymbol{\rho}}\|_{\mathbb{F}}. \quad (19)$$

The integrals presented in Eqs. (16) and (17) and consequently in (19), which are products of the tensors related to the Green's function solution, $\boldsymbol{\Gamma}^\infty$ and $\boldsymbol{U}^\infty$, and the second-order probability function, are strenuous especially near the origin due to the singularity of $\boldsymbol{\Gamma}^\infty$ and $\boldsymbol{U}^\infty$. Note that, for statistically isotropic systems and systems with aligned ellipsoids, these integrals can be calculated analytically leading to a closed-form solution of the overall conductivity tensor. Closed-form solutions using these assumptions have been presented in work by Willis [30] and Weng [61], just to name a few. This work is not limited by these assumptions, and the integral kernels are calculated numerically using the adaptive sparse-grid Smolyak integration method with hierarchical basis that was developed in our previous work [44].

IV. STATISTICAL CHARACTERIZATION

After the voxel data is processed, the packs are statistically characterized by computing one- and two-point probability functions directly from the voxel data using our parallel statistical sampling code, STAT3D [20]. Note that sampling in $\mathbb{R}^3$ on idealized packs as done in [20] is also possible and would result in nearly identical results as shown in [26]. We do not present this verification here. This section presents the statistical functions for compositions described in Sec. II E. The semiordered pack and one realization of each randomized composition [higher volume fraction packs as shown in Fig. 12(a)] are statistically characterized.

As presented in [20], a spherical sampling template is used to compute n-point probability functions. After a convergence study, the sampling template was discretized with 2000 radial points and 32 circumferential points and was randomly thrown into the sample 10 million times. Note that this very high sampling frequency is important for resolving all probability functions. In order to quantify the errors in the statistical functions, we consider the limit cases of the two-point

probability functions as given by Eq. (11). The following error measures at the origin and at a far distance are used,

$$0 \leqslant \varepsilon_{S_{rs}(\mathbf{0})} = \frac{\left| S_{rs}(\mathbf{0}) - c_r^v \delta_{rs} \right|}{c_r^v} \times 100[\%], \qquad (20)$$

$$0 \leqslant \varepsilon_{S_{rs}(\infty)} = \frac{\text{std}\left[S_{rs}(\infty) - c_r^v c_s^v \right]}{c_r^v c_s^v} \times 100[\%], \qquad (21)$$

where std($\bullet$) is the standard deviation.

If a pack is perfectly isotropic, the standard deviations in the two-point probability functions at $|\mathbf{x} - \mathbf{x}'|$ are zero (std$[S_{rs}(\mathbf{x} - \mathbf{x}')]|_{|\mathbf{x}-\mathbf{x}'|} = 0 \ \forall \mathbf{x}$). For random statistically homogeneous mixtures, short-range statistical anisotropy can exist due to both the shape of the particles and/or the configuration of the particles, and no long-range order is expected for randomized systems. A specific case of statistically anisotropic systems, considered in previous works [29,30], is when the two-point probability functions exhibit ellipsoidal symmetry, which is known to occur for ordered packs of randomly positioned and uniformly aligned monodisperse ellipsoids. Ellipsoidal symmetry means that the function values of $S_{rs}(\mathbf{x} - \mathbf{x}')$ are constant on contours of an ellipsoid,

$$(\mathbf{x} - \mathbf{x}')^T \mathbf{B}^{-1}(\mathbf{x} - \mathbf{x}'), \qquad (22)$$

where $\mathbf{B}$ is a positive-definite matrix whose eigenvalues are squares of an ellipsoid's semiaxes. It will be shown that the statistical descriptors of the polydisperse packs in this work do not exhibit ellipsoidal symmetry. When ellipsoidal symmetry does not exist, closed-form solutions of the overall properties as presented in [30] and many papers thereafter cannot be obtained.

A. Semiordered pack

In what follows, the subscripts m, s, and e are used to refer to the matrix, spherical particles (mustard seeds), and ellipsoidal particles (rice grains), respectively. The one-point probability functions for the semiordered mixture of ellipsoids (see Fig. 9) are $c_m = 0.3345$ and $c_e = 0.6655$. The mean and standard deviations of the two-point probability functions

are presented in Fig. 16. The maximum errors, as defined by Eqs. (20) and (21) for all two-point probability functions of this mixture are $\varepsilon_{S_{rs}(\mathbf{0})} = 0.0059\%$ and $\varepsilon_{S_{rs}(\infty)} = 0.304\%$, respectively. As can be seen in Fig. 16(a), the mean two-point probability values reach local extrema near the average semi-axis, $(a + b + c)/3 = 1.66$ mm (vertical gray dotted line), and the largest semiaxis (vertical black dashed line). Note that the average semiaxes of ellipsoids in this work are $a = 3.04$ mm, $b = 1.111$ mm, and $c = 0.83$ mm. Considering the mean function values and the standard deviations as $(\mathbf{x} - \mathbf{x}') \to \infty$ (Fig. 16), the functions are considered converged when $|\mathbf{x} - \mathbf{x}'| = 8$ mm, resulting in a characteristic material length scale of 16 mm (twice the radius). The characteristic material length scale can be considered as the optimal size of a representative unit cell (RUC) [20]. This length scale is $\sim 20\times$ the smallest semiaxis and $\sim 5\times$ the largest semiaxis. The characteristic material length scale is important in this work, as the saturation of the probability functions guarantees convergence of the integrals in Eqs. (16), (17), and (19) as $(\mathbf{x} - \mathbf{x}') \to \infty$ [30]. Also of interest in Fig. 16(b) is where the maximum standard deviations occur, since the std(S_{rs}) represents how anisotropic the system is. The largest peak occurs near a distance from the origin of the smallest semiaxis ($c = 0.83$ mm), the second peak near the average semiaxis (dotted gray line), and the deviations diminish after the distance near the largest semiaxis (dashed black line). Note that these deviations are related to a combination of the particle shape, the polydispersity, and the configuration. While these deviations are less than 6% of the function values, this statistical anisotropy will lead to large macroscopic anisotropy of the thermal-conductivity tensor, because the anisotropy in morphology is amplified by the local anisotropic material constants.

One of the two-point probability functions, S_{ee}, is visualized in Fig. 17. Notice again that local minima exist near distances from the origin to the average semiaxis and the largest semiaxis lengths. The anisotropic nature of the two-point probability function in the xy and yz plane [Figs. 17(c) and 17(d), respectively] is due to the preferred alignment of the particles in the y direction (see Fig. 11). While the
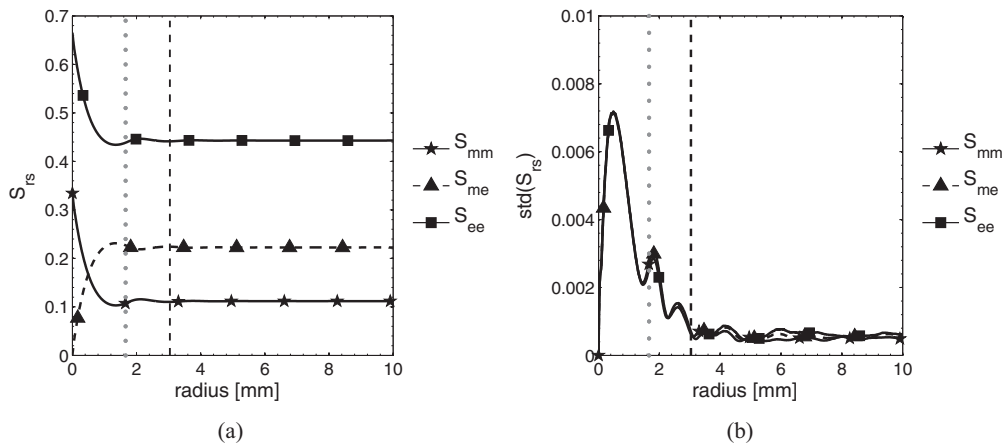

(a)

(b)

FIG. 16. (a) Mean of two-point probability functions, S_{rs}, for semiordered pack of ellipsoids from Fig. 9. (b) Standard deviation (std) of S_{rs} for semiordered pack of ellipsoids. In both (a) and (b), the vertical dotted gray line indicates the average semiaxis length [$(a + b + c)/3 = 1.66$ mm] of the ellipsoids in the pack, while the vertical dashed black line indicates the largest semiaxis length ($c = 0.83$ mm).
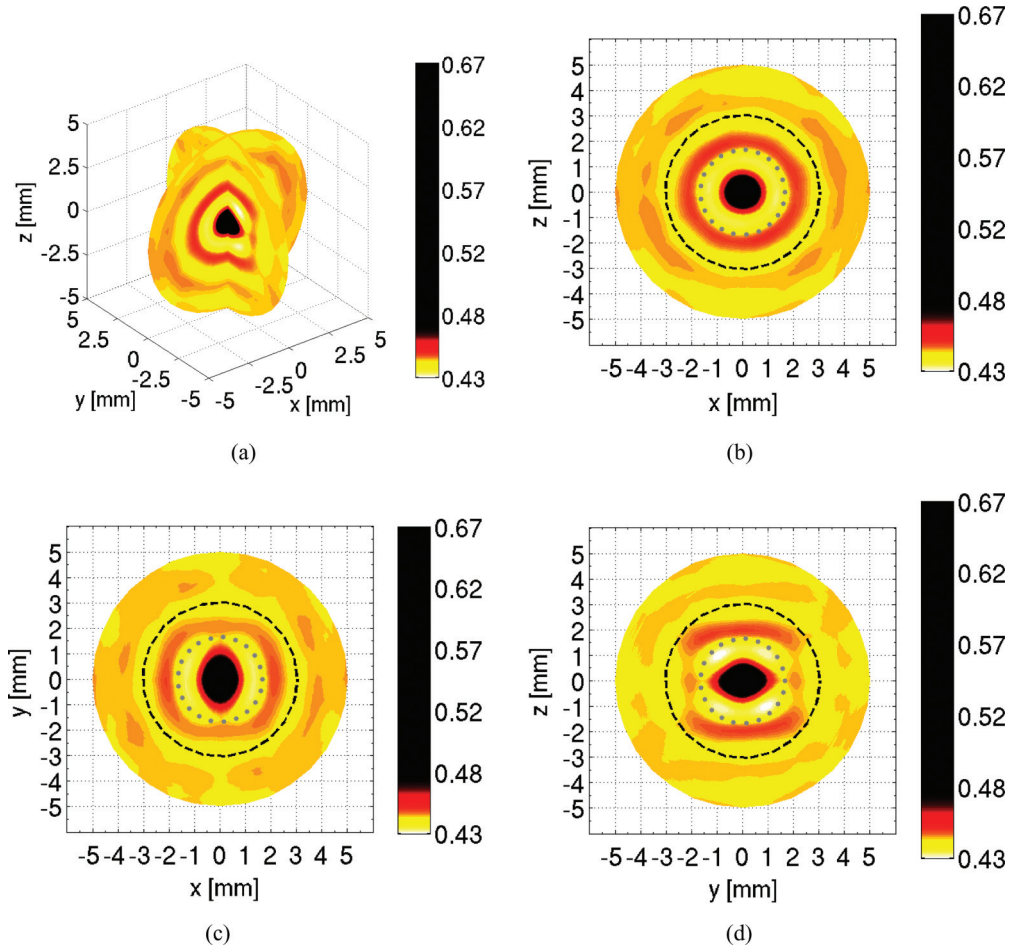
FIG. 17. (Color online) (a) 3D representation of $S_{ee}(x - x')$ for semiordered pack of ellipsoids from Fig. 9. (b)–(d) show $S_{ee}(x - x')$ in the xz, xy, and yz planes, respectively. Note that this function does not exhibit ellipsoidal symmetry. Note that the scale of the color bar is adjusted to highlight where local minima of this function exist. The dotted gray line indicates the average semiaxis length of the ellipsoids in the pack $[(a + b + c)/3 = 1.66$ mm], while the dashed black line indications the largest semiaxis length ($c = 0.83$ mm).

general shape of this statistical function is ellipsoidal, notice that S_{ee} does not exhibit complete ellipsoidal symmetry [given by Eq. (22)], thus prohibiting the closed-form integration given in [30]. Near spherical symmetry occurs only in the xz plane [Fig. 17(b)], since the smallest semiaxes of the average size ellipsoid are similar ($b = 1.11$ mm and $c = 0.83$ mm). Note that for a semiordered pack (based on our packing method, this means not randomly positioned and uniformly aligned inclusions) of ellipsoids in which all semiaxes are significantly different, ellipsoidal symmetry would not be present in any plane.

B. Randomized packs

The mean and standard deviations of the two-point probability functions for selected randomized compositions are considered in Figs. 18(a)–18(f). The maximum errors, as defined by Eqs. (20) and (21), for all two-point probability functions of the five randomized compositions are $\varepsilon_{S_{rs}(0)} = 0.104\%$ and $\varepsilon_{S_{rs}(\infty)} = 4.146\%$, respectively. Note that the spike in the standard deviations at the origin in Fig. 18(f) (less than 1% of the function value) occurs at the voxel resolution of the data set, $|x - x'| \approx 0.07$ mm. This is a numerical artifact

due to the discontinuities associated with the voxelization of data. In Fig. 18(d), the standard deviations for the 50% pack as $(x - x') \to \infty$ are not fully saturating for some functions. This indicates that larger samples might be needed for better resolution. Nevertheless, these functions are not significantly misrepresenting the statistical anisotropy in the system, since the standard deviations as $(x - x') \to \infty$ are on the same order as the standard deviation peaks near the origin. For the 25% and 75% compositions, the standard deviations as $(x - x') \to \infty$ are similar to those for the 50% mixture. The general trend shows that the maximum standard deviations for the two-point probability functions of the mixtures decrease as the amount of spheres in the system increases [Figs. 18(b), 18(e), and 18(f)], indicating the spherical particles tend to organize randomly (isotropically). For the 100% mixture of spheres, the deviations are essentially zero [Fig. 18(f)], indicating the pack is nearly isotropic. This trend in statistical anisotropy will be reflected in the macroscopic anisotropy of the thermal-conductivity tensor. Once more, individual local minima and corresponding high standard deviations are due to both particle shape and spatial organization.

Considering both the deviations as $(x - x') \to \infty$ and where the two-point probability functions saturate,
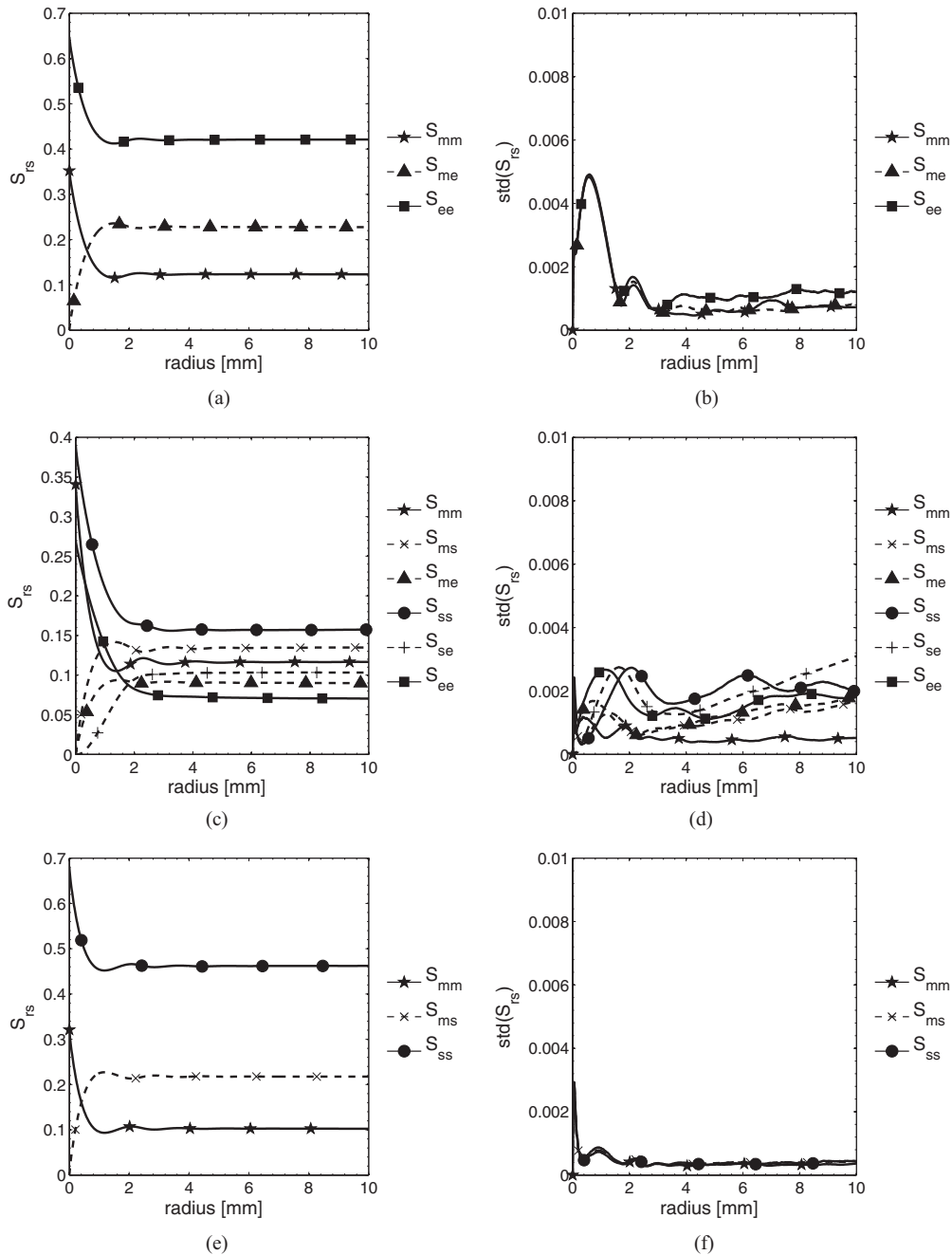
FIG. 18. Mean and standard deviations of two-point probability functions, S_{rs}, for randomized packs of 0% [(a) and (b)], 50% [(c) and (d)], and 100% [(e) and (f)] weight of spherical particles from Table I.

characteristic material length scales are determined for the mixtures. The mixtures with only one particulate phase (0% and 100% weight of spherical particles) have a characteristic material length scale around 16 mm, as the functions converge at $|\boldsymbol{x} - \boldsymbol{x}'| = 8$ mm. This same length scale is attributed to the similarity in the average semiaxis length of the ellipsoids, $(a + b + c)/3 = 1.66$ mm, and the radius of the average sphere, 0.94 mm. The three phase mixtures (25%, 50%, and 75% weight of spherical particle packs) have larger characteristic material length scales, 20 mm. This larger length scale is expected, because more interactions must be captured as polydispersity and the number of phases grow.

When comparing the probability functions of the randomized pack of 100% ellipsoids to the semiordered pack of ellipsoids, the amount of statistical anisotropy reflects the differences in configuration. The maximum standard deviation for the randomized pack of ellipsoids is $\mathrm{std}(S_{rs}) = 0.0049$ [see Fig. 18(b)], which is smaller than the maximum standard deviation of the semiordered pack $\mathrm{std}(S_{rs}) = 0.0072$ [Fig. 16(b)], and indicates less statistical anisotropy. Also note that there are only two maxima in the standard deviations as compared to three for the semiordered pack [compare Figs. 16(b) and 18(b)]. As there is no apparent alignment in the xy plane for the randomized pack (Fig. 14), the two-point

probability functions reflect this behavior and smooth out these standard deviation peaks.

V. OVERALL ANISOTROPIC PROPERTY CALCULATIONS

In this work, it is assumed that the ellipsoidal particles exhibit transverse isotropic behavior ($\{\kappa_e^{\eta_1}, \kappa_e^{\eta_2}, \kappa_e^{\eta_3}\} = \{400, 100, 100\}$ W/mK), while the matrix and spherical particle phases are isotropic ($\kappa_m = 10$ W/mK; $\kappa_s = 50$ W/mK). A volume averaged conductivity tensor for the ellipsoidal phase is computed as

$$\kappa_e(\boldsymbol{x}) = \frac{1}{\Omega_e} \int \boldsymbol{R}^T \kappa_e^{\eta} \boldsymbol{R} \chi_e(\boldsymbol{x}) d\Omega, \qquad (23)$$

where $\boldsymbol{R}$ is the rotation matrix associated with the orientation of a particle and χ_e is the indicator function for the ellipsoidal particles as defined in Eq. (7). For an isotropic distribution of transverse isotropic ellipsoidal particles, the volume averaged tensor would be isotropic with the mean thermal conductivity $\kappa_e = 200$ W/mK. This was verified by considering uniformly distributed rotation matrices for the given transverse isotropic conductivity tensor [62]. However, for an anisotropic distribution of particles, the volume averaged tensor can lead to a symmetric anisotropic conductivity tensor.

As described in Sec. III B, the integrals present in Eqs. (16), (17), and (19) are integrated numerically using the adaptive sparse-grid Smolyak integration method with hierarchical basis. As discussed in [44], the numerical accuracy depends on three parameters, namely the quality of the interpolation defined as $\hat{\varepsilon}$, the quality of the integration defined as $\tilde{\varepsilon}$, and on the convergence of the integral, $\mathcal{E}_\mathcal{I}$. The quality of the interpolation, $\hat{\varepsilon}$, is the cutoff that determines which grid points remain in the sparse grid. We use $\hat{\varepsilon} = 1 \times 10^{-8}$ and 1×10^{-4} for the lower and upper bound calculations, respectively. The quality of the integration, $\tilde{\varepsilon}$, is related to the volume removed in the integral due to the singularity and is denoted as

$$\int_{\Omega_{\boldsymbol{x}'}} \boldsymbol{\Gamma}(\boldsymbol{x} - \boldsymbol{x}')[S_{rs}(\boldsymbol{x} - \boldsymbol{x}') - c_r c_s] d\Omega_{\boldsymbol{x}'}$$
$$\approx \mathcal{I} = \int_{\Omega_{\boldsymbol{x}'}} \boldsymbol{\Gamma}_s[S_{rs}(\boldsymbol{x} - \boldsymbol{x}') - c_r c_s]\delta(\boldsymbol{x} - \boldsymbol{x}') d\Omega_{\boldsymbol{x}'}$$
$$+ \int_{\Omega_{\boldsymbol{x}'} \backslash v} \boldsymbol{\Gamma}_f(\boldsymbol{x} - \boldsymbol{x}')[S_{rs}(\boldsymbol{x} - \boldsymbol{x}') - c_r c_s] d\Omega_{\boldsymbol{x}'}. \quad (24)$$

Here, $\boldsymbol{\Gamma}_s$ and $\boldsymbol{\Gamma}_f$ denote the singular and formal terms of $\boldsymbol{\Gamma}$, and a discussion on the derivation of these terms is provided in the Appendix. $\delta(\boldsymbol{x} - \boldsymbol{x}')$ is the Dirac delta function and v is the small volume close to the singularity of $\boldsymbol{\Gamma}_f$ that we remove. This volume v is a sphere of radius $\tilde{\varepsilon}$ removed around the origin ($\boldsymbol{x} = \boldsymbol{x}'$). After a convergence study, we selected $\tilde{\varepsilon} = 0.1$ mm for all computations. All solutions are stopped when the integrals converge within a certain tolerance,

$$\mathcal{E}_\mathcal{I} = |\mathcal{I}_h - \mathcal{I}_{h-1}| / |\mathcal{I}_{h-1}| \leqslant \text{tol} = 0.001, \qquad (25)$$

where the subscript h is the sparse grid integration level (see [44] for more details). In order to quantify the overall numerical error due to the numerical parameters mentioned above, we define

$$e_n = \frac{\|\overline{\kappa}_{S_{rs}(|\boldsymbol{x} - \boldsymbol{x}'|)} - \overline{\kappa}_s\|_\mathbb{F}}{\|\overline{\kappa}_s\|_\mathbb{F}} \times 100[\%]. \qquad (26)$$

This definition takes advantage of a property of $\boldsymbol{\Gamma}_f$, where

$$\lim_{v \to 0} \int_{\Omega_{\boldsymbol{x}'} \backslash v} \boldsymbol{\Gamma}_f(\boldsymbol{x} - \boldsymbol{x}') f(\boldsymbol{x} - \boldsymbol{x}') d\Omega_{\boldsymbol{x}'} = \boldsymbol{0} \qquad (27)$$

for any statistically isotropic function, $f(\boldsymbol{x} - \boldsymbol{x}')$. In Eq. (26), $\overline{\kappa}_{S_{rs}(|\boldsymbol{x} - \boldsymbol{x}'|)}$ is computed by numerically evaluating the integral $\mathcal{I}$ with isotropic statistics, and $\overline{\kappa}_s$ is obtained in a closed form [30]. Considering Eq. (27), the overall numerical error in Eq. (26) measures the accuracy of the numerical integration of the kernel including $\boldsymbol{\Gamma}_f$ [see Eq. (24)]. Note that $\overline{\kappa}_{S_{rs}(|\boldsymbol{x} - \boldsymbol{x}'|)}$ is not a physically meaningful quantity and is only used to determine the numerical error of the calculations. All overall thermal-conductivity tensor calculations presented hereafter are computed with a numerical error $e_n < 0.16\%$. Note that we are using the material characteristic length scale to integrate over $\Omega_{\boldsymbol{x}'}$ (see discussion in Secs. IV A and IV B), and a convergence study has been performed to verify this far limit of the integration.

When computing the self-consistent estimate, the NLOPT library [63] (nonlinear optimization package) was used for minimizing the objective functions [Eq. (19)]. For this work, the objective function is considered converged when the function value is less than 1×10^{-6}. Note that the objective function is approaching 0 as $\kappa_0 \to \overline{\kappa}$. It has been confirmed that the self-consistent estimates using both the upper and lower formulations of $\overline{\kappa}$ [see Eq. (19)] yield identical results. This is another verification test.

The resulting bounds and self-consistent estimate of the overall anisotropic thermal-conductivity tensor for the semiordered pack of ellipsoids are listed in Table III, where the eigenvalues of the overall conductivity tensor are presented. The eigenvalues of the conductivity tensor ($\overline{\kappa}_1$, $\overline{\kappa}_2$, and $\overline{\kappa}_3$) correspond to the components of the conductivity tensor in the principal coordinate frame, where the material behaves as an orthotropic one. $\overline{\kappa}_i$ (subscript i stands for isotropic) refers to the assumption that the particles are isotropically distributed (perfectly random), with $\kappa_e = 200$ W/mK, leading to a macroscopically isotropic conductivity tensor with one independent component ($\overline{\kappa}_1 = \overline{\kappa}_2 = \overline{\kappa}_3$). $\overline{\kappa}_i$ is calculated in a closed form. $\overline{\kappa}_a$ is the anisotropic conductivity tensor (subscript a stands for anisotropic), which considers both the anisotropic constituent

TABLE III. Overall thermal-conductivity tensor, $\overline{\kappa}$, for semiordered pack from Fig. 9. Note that the subscript i refers to an assumed isotropic distribution of the particles, while the subscript a refers to anisotropic morphology. The numeral subscripts (1, 2, and 3) refer to the eigenvalues of the resulting thermal-conductivity tensor in the principal coordinate frame.

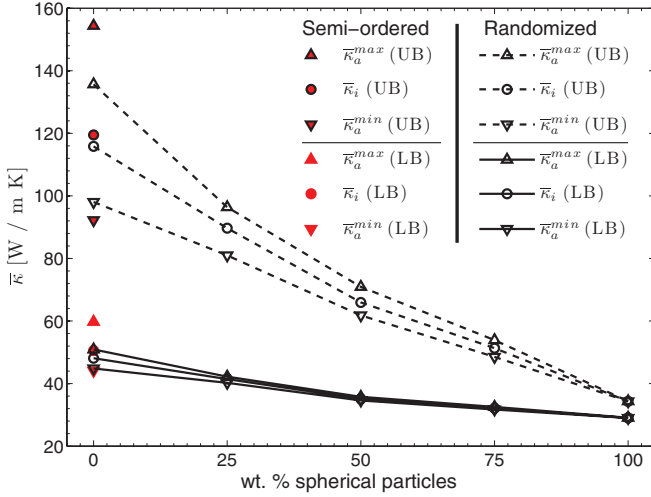|	$\overline{\kappa}_1$ [W/mK]	$\overline{\kappa}_2$ [W/mK]	$\overline{\kappa}_3$ [W/mK]	Mean($\overline{\kappa}_1, \overline{\kappa}_2, \overline{\kappa}_3$)
	Isotropic distribution of particles			
$\overline{\kappa}_i$ (LB)			50.55	
$\overline{\kappa}_i$ (SC)			108.85	
$\overline{\kappa}_i$ (UB)			119.47	
	Anisotropic model			
$\overline{\kappa}_a$ (LB)	59.74	48.47	44.11	50.77
$\overline{\kappa}_a$ (SC)	141.45	99.65	85.27	108.79
$\overline{\kappa}_a$ (UB)	154.39	109.26	92.23	118.62

FIG. 19. (Color online) Upper bound (UB) and lower bound (LB) calculations of thermal conductivity, $\overline{\kappa}$, for all randomized compositions from Table I and semiordered pack of ellipsoids from Fig. 9. Note that the subscript i refers to an assumed isotropic distribution of the particles, while the subscript a refers to anisotropic morphology. The superscripts min and max refer to the smallest and largest eigenvalue of the thermal-conductivity tensor in the principal coordinate frame, respectively.

and statistically anisotropic configuration. $\overline{\kappa}_a$ is calculated numerically [44].

As can be seen in Table III, the components of the anisotropic thermal-conductivity tensor vary significantly. For example, in the upper bound of $\overline{\kappa}_a$, the difference between the minimum and maximum eigenvalue is $154.39 - 92.23 = 62.16$ W/mK. For the lower bound of $\overline{\kappa}_a$, we obtain $59.74 - 44.11 = 15.63$ W/mK. While the standard deviations in the statistical functions were moderate (see Fig. 16), these deviations have a significant effect on the overall material behavior as they are magnified by the anisotropy in $\boldsymbol{\kappa}_e$ [see Eq. (23)]. Note that the mean of the eigenvalues of $\overline{\kappa}_a$ is nearly identical to results for $\overline{\kappa}_i$ for all three models (UB, LB, and SC), which confirms numerical accuracy.

The resulting upper and lower bounds of the thermal-conductivity tensor for the five randomized packs and the semiordered pack are presented in Fig. 19. Here, $\overline{\kappa}^{\max,\min}$ refers to the maximum and minimum eigenvalue of the overall conductivity tensor. These maximum and minimum conductivity components (solid lines with triangles for LB and dashed lines with triangles for UB) are compared to those assuming an isotropic distribution of particles, $\overline{\kappa}_i$ (solid line with circles for LB and dashed line with circles for UB). Note that $\overline{\kappa}_i$ (UB) and $\overline{\kappa}_i$ (LB) were computed with $\kappa_2 = 200$ W/mK. In general, the spread of the bounds increases for packs with more ellipsoidal particles, because the difference between the conductivities of an ellipsoidal particle and the matrix is larger than the difference between the conductivities of a sphere and the matrix (see lines with circles in Fig. 19). Also note that the spread in the minimum and maximum components of $\overline{\kappa}_a$ for both bounds increases for packs with more ellipsoidal particles due to the increasing amount of statistical anisotropy present in the packs. Recall that the statistical anisotropy was quantified based on the standard deviations in the two-point

probability functions [see Figs. 18(b), 18(d), and 18(f)]. The spread in the components of the conductivity tensor for the lower bound is smaller than the spread for the upper bound, since the least conductive constituent (matrix) is isotropic and the most conductive constituent (ellipsoids) is anisotropic.

When comparing the semiordered pack of ellipsoids (filled markers on the left in Fig. 19) to the randomized pack of ellipsoids, first note that the semiordered pack has a larger $\overline{\kappa}_i$ than the randomized pack, because the semiordered system has a higher packing fraction (see Sec. II E 2). Also note that the spread of the conductivity components is larger for the semiordered pack due to the larger statistical anisotropy present in the semiordered pack [compare Figs. 16(b) and 18(b)]. We will comment on the extent of these differences when we introduce a measure of anisotropy below.

The self-consistent estimates for the mixtures are presented in Fig. 20. The same trends described for Fig. 19 are observed. In order to compare the self-consistent estimates to the LB and UB computations, we also show the isotropic LB and UB behavior, respectively. Note that the self-consistent estimates are closer to the upper bound calculations, since this second-order model is strongly dependent on the volume fraction, and all of the packs have volume fractions greater than 0.6. Also note that there is no restriction on the self-consistent estimate being between the lower and upper bounds.

In order to quantify the macroscopic anisotropy of the thermal-conductivity tensor, a measure of anisotropy, M_A, is defined as

$$M_A = \max\left(\left|\overline{\kappa}_a^{\max} - \overline{\kappa}_i\right|, \left|\overline{\kappa}_a^{\min} - \overline{\kappa}_i\right|\right) \Big/ \overline{\kappa}_i \times 100[\%]. \quad (28)$$
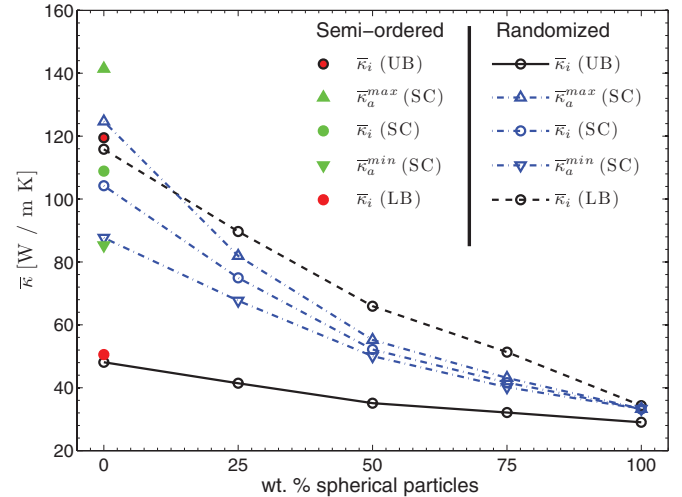

FIG. 20. (Color online) Self-consistent (SC) estimates of thermal conductivity, $\overline{\kappa}$, for all randomized compositions from Table I and semiordered pack of ellipsoids from Fig. 9. The results are compared to the upper bound (UB) (dashed line with circles) and lower bound (LB) (solid line with circles) isotropic calculations. Note that the subscript i refers to an assumed isotropic distribution of the particles, while the subscript a refers to anisotropic morphology. The superscripts min and max refer to the smallest and largest eigenvalue of the thermal-conductivity tensor in the principal coordinate frame, respectively.
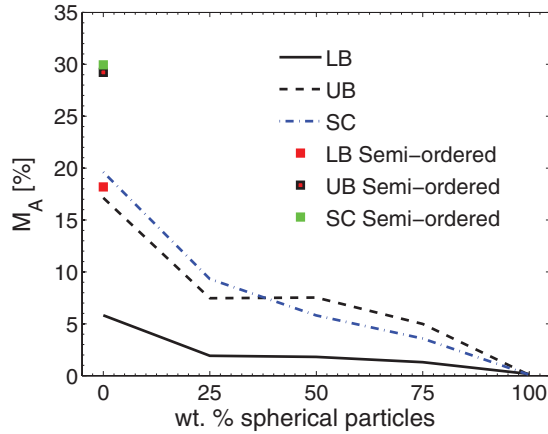
FIG. 21. (Color online) Measure of anisotropy, M_A [Eq. (28)], for lower bound (LB), upper bound (UB), and self-consistent (SC) calculations of all compositions considered.

Computed measures of anisotropy for results in Figs. 19 and 20 are presented in Fig. 21. As alluded to above, the measure of anisotropy increases as more ellipsoidal particles are present due to the increasing statistical anisotropy in the system. Let us consider the measure of anisotropy for the upper bound (dashed black line in Fig. 21). Here $M_A = 0.08\%$ for the 100% mixture (all spheres) and increases up to $M_A = 17.14\%$ for the 0% mixture (all ellipsoids). For the lower bound, M_A grows from $M_A = 0.16\%$ to $M_A = 5.82\%$. The measures of anisotropy of the upper and lower bounds for the 100% mixture (all spheres) are near the numerical error, $|M_A(UB) - M_A(LB)| = 0.08\%$ ($e_n = 0.16\%$). Note that the anisotropic upper and lower bounds are rigorous bounds on the overall anisotropic thermal-conductivity tensor. Therefore, these upper and lower bounds also provide limits on the measure of anisotropy. For example, the anisotropy of the 0% mixture (all ellipsoids) falls between $M_A = 5.82\%$ (LB) and $M_A = 17.14\%$ (UB).

The measures of anisotropy for the semiordered pack (filled markers in Fig. 21) are significantly larger than the estimates of the randomized packs and are bounded between $M_A = 18.19\%$ (LB) and $M_A = 29.23\%$ (UB). Let us consider the upper bound results, where $M_A = 29.23\%$ for the semiordered pack [red (gray) filled square with black outline in Fig. 21] as compared to $M_A = 17.14\%$ for the randomized pack of ellipsoids (dashed black line at 0 wt % spherical particles in Fig. 21), and let us contrast those to std(S_{rs}) = 0.0072 for the semiordered pack and std(S_{rs}) = 0.0049 for the randomized pack [see Figs. 16(b) and 18(b) in Sec. IV]. Note that the measure of anisotropy for the self-consistent estimates of the 0% and 25% mixtures (blue dotted dashed line) is higher than the anisotropy in the upper bound (black dashed line). Just as a self-consistent estimate is not guaranteed to be between the upper and lower bounds, the measure of anisotropy associated with this estimate is not expected to be between the upper and lower bounds.

VI. CONCLUSIONS

In this work, we present a systematic microstructure characterization procedure anchored in micro-CT data that is used to establish microstructure-statistics-property relations of polydisperse particulate mixtures. An image processing pipeline is developed that accurately identifies particles while maintaining low errors. Improvements in the image processing pipeline are achieved when compared to a traditional technique. For all compositions considered, the volume losses due to image segmentation are less than 4%. These low errors indicate that scientifically sound and repeatable results have been achieved. Next, we developed a description of the polydisperse system in continuous Euclidean space. This idealized representation provides a substantial reduction in the data set size and enables easier data manipulation and understanding.

After characterizing the microstructure, three-dimensional n-point probability functions of real polydisperse mixtures are calculated. We show that second-order probability functions do not exhibit ellipsoidal nor any other material symmetry. Therefore, assessment of overall material constants in a closed form is unattainable.

The statistical description is then used to compute bounds and self-consistent estimates of the anisotropic thermal-conductivity tensor using the Hashin-Shtrikman variational principle. The anisotropic second-order estimates of polydisperse composites are calculated without assumptions on an inclusion's shape, configuration, and/or material anisotropy. The overall properties show increasing anisotropy in the overall thermal-conductivity tensor for packs with more transverse isotropic ellipsoidal inclusions. Moreover, the upper and lower bounds provide limits on the anisotropy of the mixtures. Due to the larger amounts of statistical anisotropy for the semiordered mixture, the measure of anisotropy for the overall conductivity tensor of this pack was significantly larger than for the randomized one.

APPENDIX: DISCUSSION ON $\Gamma(x, x')$

The infinite homogeneous Green's function for steady-state heat conduction of an anisotropic material is

$$g(x - x') = \frac{1}{(d - 2)\Omega(d)R}\det(\kappa^{-1}), \quad (A1)$$

where det($\bullet$) stands for the determinant, $R = [(x - x') \cdot \kappa \cdot (x - x')]^{1/2}$, $d = 3$ is the dimension, and $\Omega(d)$ is the total solid angle in a d-dimensional sphere [64,65]. Following the work of Torquato [66], $\Gamma(x - x')$ is obtained by first considering a temperature field defined as

$$T(x) = T_0(x) - \int_{\Omega_{x'}} \nabla g(x - x') \cdot p(x')d\Omega. \quad (A2)$$

After integrating this equation by parts, using the Gauss-divergence theorem, and excluding a small spherical region

around $x = x'$, one obtains

$$\mathbf{Q} = \mathbf{Q}_0 - \int_{\Omega_{x'}} \mathbf{\Gamma}(\mathbf{x} - \mathbf{x}') \cdot \mathbf{p}(\mathbf{x}') d\Omega. \tag{A3}$$

The resulting $\mathbf{\Gamma}(\mathbf{x} - \mathbf{x}')$ used in Eq. (16) is defined as

$$\mathbf{\Gamma}(\mathbf{x} - \mathbf{x}') = \mathbf{\Gamma}_f(\mathbf{x} - \mathbf{x}') + \mathbf{\Gamma}_s \delta(\mathbf{x} - \mathbf{x}'), \tag{A4}$$

where

$$\mathbf{\Gamma}_s = \int_{|\mathbf{x} - \mathbf{x}'| = R_s} (g_{,i}\hat{n}_j + g_{,j}\hat{n}_i) d\Omega \tag{A5}$$

and

$$\mathbf{\Gamma}_f(\mathbf{x} - \mathbf{x}') = -\frac{\partial^2 g}{\partial x_i \partial x_j}. \tag{A6}$$

Here, the unit normal $\hat{\mathbf{n}}$ is the unit normal of the spherical surface ($|\mathbf{x} - \mathbf{x}'| = R_s$) over which the integration occurs. For an isotropic constituent, $\mathbf{\Gamma}_s$ can be integrated analytically, while obtaining an analytical solution becomes increasingly difficult for an anisotropic one. In this work, the singular term is computed numerically using an adaptive multidimensional integration scheme provided as an extension to the GNU Scientific Library (GSL). The singular term is calculated until the relative error of the integral is less than 1×10^{-5}. Note that the integral of $\mathbf{\Gamma}_f(\mathbf{x} - \mathbf{x}')$ over the surface of a sphere is zero,

$$\int_{|\mathbf{x} - \mathbf{x}'| = R_s} \mathbf{\Gamma}_f(\mathbf{x} - \mathbf{x}') d\Omega = \mathbf{0}. \tag{A7}$$

[1] P. Chaikin and T. Lubensky, *Principles of Condensed Matter Physics* (Cambridge University Press, New York, 2000).

[2] S. Torquato, *Random Heterogeneous Materials* (Springer, New York, 2002).

[3] K. Matouš, H. Inglis, X. Gu, D. Rypl, T. Jackson, and P. Geubelle, Compos. Sci. Technol. **67**, 1694 (2007).

[4] J. Andrade and X. Tu, Mech. Mater. **41**, 652 (2009).

[5] J. Liang and K. Dill, Biophys. J. **81**, 751 (2001).

[6] X. Fu, M. Dutt, A. C. Bentham, B. C. Hancock, R. E. Cameron, and J. A. Elliott, Powder Technol. **167**, 134 (2006).

[7] M. Tixier, O. Pitois, and P. Mills, Eur. Phys. J. E **14**, 241 (2004).

[8] A. Liu and S. Nagel, Annu. Rev. Condens. Matter Phys. **1**, 347 (2010).

[9] P. Cleary and M. Sawley, Appl. Math. Model. **26**, 89 (2002).

[10] Y. Fu, Y. Xi, Y. Cao, and Y. Wang, Phys. Rev. E **85**, 051311 (2012).

[11] P. Ribière, P. Richard, R. Delannay, and D. Bideau, Phys. Rev. E **71**, 011304 (2005).

[12] P. Breton, D. Ribereau, C. Marraud, and P. Lamarque, Int. J. Energet. Mater. Chem. Propul. **5**, 132 (2002).

[13] J. Gevertz and S. Torquato, PLoS Comput. Biol. **4**, e1000152 (2008).

[14] A. U. Nilsen and P. J. Monteiro, Cem. Concr. Res. **23**, 147 (1993).

[15] S. Gallier and F. Hiernard, J. Propul. Power **24**, 147 (2008).

[16] B. Collins, F. Maggi, K. Matouš, T. Jackson, and J. Buckmaster, in *46th AIAA Aerospace Sciences Meeting and Exhibit* (AIAA, Reno, NV, 2008), paper No: AIAA 2008-941.

[17] G. T. Seidler, G. Martinez, L. H. Seeley, K. H. Kim, E. A. Behne, S. Zaranek, B. D. Chapman, S. M. Heald, and D. L. Brewe, Phys. Rev. E **62**, 8175 (2000).

[18] P. Richard, P. Philippe, F. Barbe, S. Bourlès, X. Thibault, and D. Bideau, Phys. Rev. E **68**, 020301 (2003).

[19] T. Aste, M. Saadatfar, and T. J. Senden, Phys. Rev. E **71**, 061302 (2005).

[20] H. Lee, M. Brandyberry, A. Tudor, and K. Matouš, Phys. Rev. E **80**, 061301 (2009).

[21] C. Arns, M. Knackstedt, and W. Pinczewski, Geophysics **67**, 1396 (2002).

[22] J. Bernal, Nature (London) **183**, 141 (1959).

[23] M. B. Weissman, Annu. Rev. Mater. Sci. **26**, 395 (1996).

[24] J. Schmalzing and K. M. Górski, Mon. Not. R. Astron. Soc. **297**, 355 (1998).

[25] H. L. Frisch and F. H. Stillinger, J. Chem. Phys. **38**, 2200 (1962).

[26] C. Coker and S. Torquato, J. Appl. Phys. **77**, 6087 (1995).

[27] C. L. Y. Yeong and S. Torquato, Phys. Rev. E **58**, 224 (1998).

[28] D. T. Fullwood, S. R. Niezgoda, and S. R. Kalidindi, Acta Mater. **56**, 942 (2008).

[29] Z. Hashin and S. Shtrikman, J. Mech. Phys. Solids **10**, 335 (1962).

[30] J. Willis, J. Mech. Phys. Solids **25**, 185 (1977).

[31] A. Bensoussan, J. Lions, and G. Papanicolaou, *Asymptotic Analysis for Periodic Structures* (North-Holland, New York, 1978).

[32] R. Hill, Math. Proc. Cambr. Philos. Soc. **98**, 579 (1985).

[33] S. Torquato, Phys. Rev. Lett. **79**, 681 (1997).

[34] R. Christensen and K. Lo, J. Mech. Phys. Solids **27**, 315 (1979).

[35] G. Dvorak and M. Srinivas, J. Mech. Phys. Solids **47**, 899 (1999).

[36] D. Fullwood, B. Adams, and S. Kalidindi, J. Mech. Phys. Solids **56**, 2287 (2008).

[37] L. Walpole, J. Mech. Phys. Solids **14**, 151 (1966).

[38] J. Zeman and M. Šejnoha, J. Mech. Phys. Solids **49**, 69 (2001).

[39] W. Drugan and J. Willis, J. Mech. Phys. Solids **44**, 492 (1996).

[40] S. Torquato and A. K. Sen, J. Appl. Phys. **67**, 1145 (1990).

[41] P. P. Castaneda, Phys. Rev. B **57**, 12077 (1998).

[42] D. Talbot and J. Willis, J. Mech. Phys. Solids **45**, 87 (1997).

[43] R. Caulkin, X. Jia, C. Xu, M. Fairweather, R. A. Williams, H. Stitt, M. Nijemeisland, S. Aferka, M. Crine, A. Leonard, D. Toye, and P. Marchot, Ind. Eng. Chem. Res. **48**, 202 (2009).

[44] H. Lee, A. Gillman, and K. Matouš, J. Mech. Phys. Solids **56**, 1838 (2011).

[45] G. D. Scott and D. M. Kilgour, J. Phys. D **2**, 863 (1969).

[46] J. Baker and A. Kudrolli, Phys. Rev. E **82**, 061304 (2010).

[47] J. Russ, *The Image Processing Handbook* (Taylor & Francis, London, 2006).

[48] V. I. Inc., *Amira* http://www.amira.com/

[49] B. microCT, *Skyscan: Microtomography, Nanotomography, Non-invasive 3d Xray Microscopy*, http://www.skyscan.be/home.htm

[50] K. Preston and M. Onoe, *Digital Processing of Biomedical Images* (Plenum, New York, 1976).

[51] G. Windreich, N. Kiryati, and G. Lohmann, Pattern Recognit. **36**, 2531 (2003).

[52] J. Lindblad, Image Vision Comput. **23**, 111 (2005).

[53] P. M. Chaikin, A. Donev, W. Man, F. H. Stillinger, and S. Torquato, Ind. Eng. Chem. Res. **45**, 6960 (2006).

[54] T. C. Hales, Ann. Math. **162**, 1065 (2005).

[55] R. K. McGeary, J. Am. Ceram. Soc. **44**, 513 (1961).

[56] A. Donev, F. H. Stillinger, P. M. Chaikin, and S. Torquato, Phys. Rev. Lett. **92**, 255506 (2004).

[57] A. Donev, R. Connelly, F. H. Stillinger, and S. Torquato, Phys. Rev. E **75**, 051304 (2007).

[58] F. Maggi, S. Stafford, T. L. Jackson, and J. Buckmaster, Phys. Rev. E **77**, 046107 (2008).

[59] M. Beran, *Statistical Continuum Theories* (Interscience Publishers, New York, 1968).

[60] L. Onsager, Phys. Rev. **37**, 405 (1931).

[61] G. Weng, Int. J. Eng. Sci. **30**, 83 (1992).

[62] J. Arvo, *Graphic Gems III*, edited by David Kirk (Academic Press Professional, Inc., San Diego, CA, 1992), Chap. III, Sec. III.4, Fast random rotation matrices, pp. 117–120.

[63] S. G. Johnson, *The nlopt nonlinear-optimization package*, http://ab-initio.mit.edu/nlopt

[64] H.-Y. Kuo and T. Chen, Int. J. Solids Struct. **42**, 1111 (2005).

[65] Y. Chang, C. Kang, and D. J. Chen, Int. J. Heat Mass Transf. **16**, 1905 (1973).

[66] S. Torquato, J. Mech. Phys. Solids **45**, 1421 (1997).